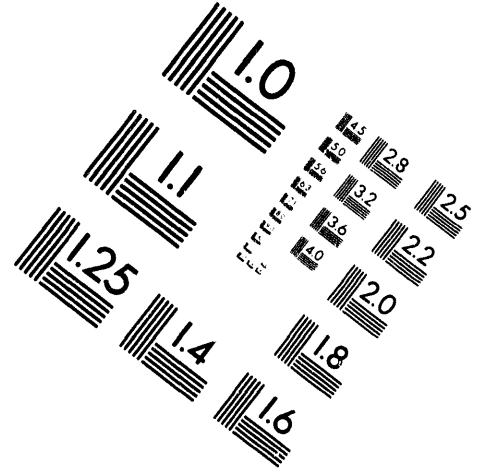
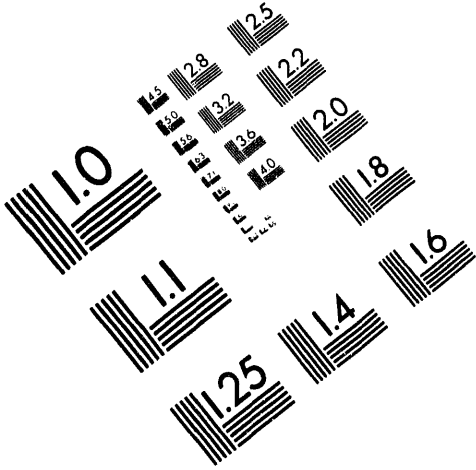




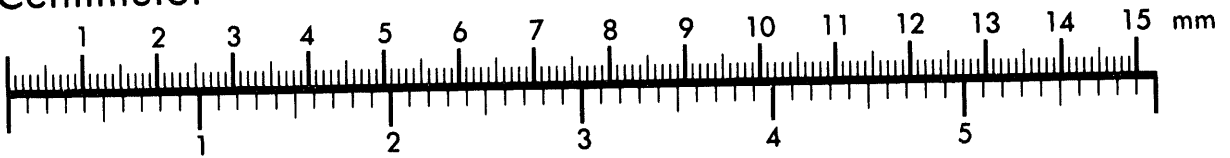
**AIM**

**Association for Information and Image Management**

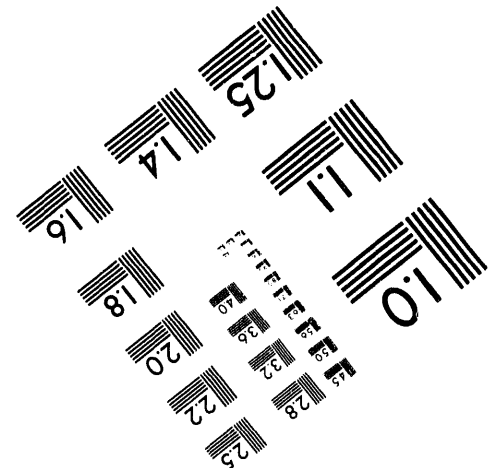
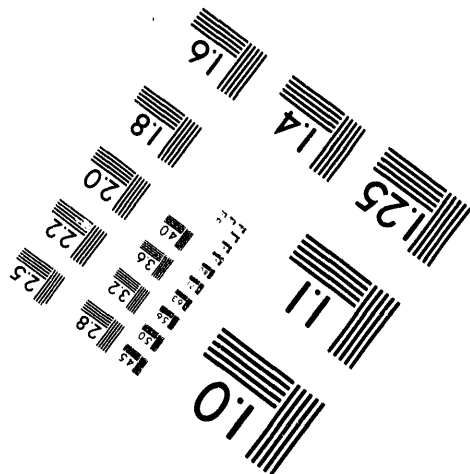
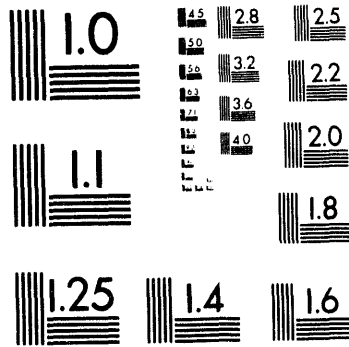
1100 Wayne Avenue, Suite 1100  
Silver Spring, Maryland 20910  
301/587-8202



**Centimeter**



**Inches**



MANUFACTURED TO AIM STANDARDS  
BY APPLIED IMAGE, INC.

**1 of 1**

## X-band microwave backscattering from ocean waves

P.H.Y. Lee, J.D. Barter, K.L. Beach, C.L. Hindman,  
B.M. Lake, H. Rungaldier, J.C. Shelton,  
A.B. Williams, R. Yee and H.C. Yuen

TRW Space and Electronics, R1-1008  
One Space Park, Redondo Beach,  
California 90278

January 4, 1994

Paper prepared for submission to *Radio Science*

Work supported by  
Office of Under Secretary of Defense/ Naval Warfare and Mobility  
under contract with  
Lawrence Livermore National Laboratory  
Subcontract B157282

DISTRIBUTION OF THIS DOCUMENT IS UNLIMITED

*for* MASTER

# X-band Microwave Backscattering from Ocean Waves

P.H.Y. Lee, J.D. Barter, K.L. Beach, C.L. Hindman, B.M. Lake, H. Rungaldier,  
J.C. Shelton, A.B. Williams, R. Yee and H.C. Yuen

TRW Space & Electronics, R1-1008, One Space Park, Redondo Beach, California

Backscattering experiments at microwave frequencies were conducted off the west coast of Scotland in the summer of 1991. Using a dual-polarization, 8-frequency X-band coherent scatterometer mounted on the bow of a boat, we measured time-resolved backscattering from ocean waves at a range of grazing angles from  $10^\circ$  to  $70^\circ$ . From the grazing-angle-dependent signals and their Doppler spectra, we differentiate Bragg scattering from non-Bragg scattering and resolve "peak separation" between the vertical and horizontal polarizations. We observe instances of "super" events, i.e., instances when the horizontal polarization return power equals or exceeds the vertical polarization power. We find that "super" events occur not only at low grazing angles but at *any* grazing angle for against-wind viewing directions. Statistics for such occurrences as a function of grazing angle are obtained. We study the coherence properties of scatterers and find strong evidence that at low grazing angles, lifetime-dominated, non-Bragg scattering contributes noticeably to returns of both polarizations, but is dominant in providing returns for the horizontal polarization. We examine "spiking" events and find that they can be related to, but need not be limited to, breaking wave events. By comparing the data of against-wind runs with cross-wind and circle runs, we obtain wind-direction dependence of Doppler spectra which further assists in the identification of scattering mechanisms.

## 1. Introduction

During the month of July, 1991, we participated in a series of experiments at Loch Linnhe and the Sound of Sleat in western Scotland. During that time, we conducted microwave backscattering experiments from wind-wave surfaces for different wind conditions at a variety of grazing angles. The objective of our experiment was to obtain a data base to facilitate the evaluation of hydrodynamic-electromagnetic interaction models in order to gain a better understanding of the physics of backscattering of microwaves from ocean surfaces in general, and of low-grazing-angle (LGA) backscattering in particular. Historically, experiments on LGA backscattering have provided the scattering community with some rather peculiar results.<sup>1-6</sup> These results have challenged theoreticians for some time and in spite of rather intense study in past and recent years, the problems of LGA scattering have proven to be remarkably resistant to analytical solution. In order to correctly model the problem, the underlying physics must first be thoroughly understood. Our approach is therefore to conduct experiments which we hope will identify the fundamental scattering mechanisms.

## 2. The microwave scatterometer

Our principal instrument for microwave measurements is a CW, dual-polarization, X-band scatterometer, designed to operate at four nominal frequency pairs:

	<u>Vertical Polarization</u>	<u>Horizontal Polarization</u>
1st pair:	9.020 GHz	9.021 GHz
2nd pair:	9.170	9.171
3rd pair:	9.320	9.321
4th pair:	9.470	9.471

The close frequency spacing between polarization channels in a pair facilitates the polarization-ratio measurement while the wide spacing between pairs provides rapid speckle averaging. In order to avoid interference from X-band equipment used by other participants in the Scotland experiment, the actual frequencies used in the field differed slightly from the nominal values.

A block diagram of the X-band scatterometer is shown in Figure 1. The two 25 cm diameter corrugated horns, separated by 28 cm (center-to-center), have a "toe-in" angle of 1.09°. The total transmitted power of the scatterometer is one watt. The receiver

preamplifier noise figure is  $2.1\text{ dB}$ . Microwave relays are used to switch the radar from an operating configuration to an internal calibration configuration where the transmitter and receiver are connected to each other *via* a  $60\text{ dB}$  attenuator, or to a null configuration where both transmitter and receiver are connected to resistive terminations. An additional set of relays are provided which can reconfigure the radar to measure cross-polarized scattering (VH, HV), however only the co-polarized (HH, VV) capability was used in the '91 experiment. Programmable attenuators are provided between the receiver horn and the low-noise amplifier of each polarization. These attenuators were set for each grazing angle and sea state to keep the recorded signal on scale. The complete scatterometer system, contained in a water-proof metal box, was mounted on an extended platform on the starboard side of the bow of an 80-ton, 24 m long research vessel. The scatterometer could be rotated about a hinge (located at the bottom of the box, 2.275 m above the mean water surface) which allowed the grazing angle to be varied.

The scattered signals of each polarization are detected by four quadrature mixers, one for each transmitted frequency. Each mixer generates an in-phase (I) and quadrature (Q) signal with a frequency response of 0 to 1000 Hz. With complex amplitude thus generated for each frequency, there are 16 channels of output. During an experiment, the sixteen signals are recorded digitally on a multichannel cassette recorder.

An absolute calibration of the scatterometer system<sup>7</sup> was conducted in a large ( $10\text{ m} \times 10\text{ m} \times 30\text{ m}$ ) anechoic chamber using spheres and cylinders of various sizes as well as corner reflector targets. Measurements consisted of establishing the output power and receiver gain of each of the eight frequency channels, the system radiation patterns in two perpendicular planes in the forward half sphere, the range dependence of the signal power, and the cross-polarization isolation of the scatterometer system. The essential results of the calibration are:

total power (8 channels) :	~ 1 W
nominal receiver gain each channel:	~ 60 dB
system radiation pattern:	approx. Gaussian main lobe
azimuthal plane -3 dB beamwidth:	$8.7^\circ$ for VV, $10.3^\circ$ for HH
vertical plane -3 dB beamwidth:	$11^\circ$ for VV, $9.6^\circ$ for HH
average -3 dB beamwidth:	$9.5^\circ$
antenna gain:	26.6 dB
cross-polarization isolation:	> 35 dB
image rejection ratio:	~ -45 dB

As an example, the measured two-way antenna pattern in the azimuthal plane (the plane containing the scatterometer boresight and the line connecting the centers of both horns) is shown in Figure 2. Note the relatively good symmetry between HH and VV patterns. Also note that the two-way side-lobes are small ( $< -65\text{ dB}$ ).

Besides the microwave scatterometer used for the present experiment, we also fielded a surface truth sensor package which contained a scanning laser slope gauge,<sup>8</sup> capacitance wire wave-height gauges, and other diagnostics which measured meteorological conditions, sea state, bulk water parameters and ship velocity.<sup>9</sup>

### 3. Experiments and data processing

Once per day during field experiments, an internal calibration sequence was recorded on tape. This sequence consisted of ten seconds each of the calibration configuration and the null configuration, while stepping the V and H input attenuators through their 0 to 70 dB span. Also, a one-time radiometric field calibration was performed using a small test sphere as a moving target.

The scatterometer data from actual ocean backscattering runs were recorded at a sampling rate of 5 kHz and down-sampled to 1.25 kHz for analysis. Preliminary data reduction included high pass filtering to eliminate DC offsets and static returns, and low-pass filtering with decimation to restrict the Doppler range to  $\pm 3.25\text{ m/s}$ . Final data reduction techniques were tailored to each of the various results. We will present speckle-averaged, time-resolved return losses, and time-resolved as well as time-averaged return loss spectral densities (Doppler spectra) for both HH and VV polarizations. Return loss refers to the ratio of the received signal to the transmitted signal and is thus specific to the scatterometer system. Its absolute measurement depends on the calibration data. The absolute radar cross section per unit area of scattering surface is obtained from the return loss using the measured antenna pattern mentioned in the previous section.

The scattering-object velocity in the water frame of reference (i.e., horizontal reference frame) is obtained from the Doppler frequency given by

$$f_D = \frac{2 \cos \theta_g}{\lambda} (v_b \pm v_d \pm v_c \pm c_p), \quad (1)$$

where  $\theta_g$  is the scatterometer local grazing angle,  $\lambda$  is the microwave freespace wavelength,  $v_b$ ,  $v_d$ ,  $v_c$  and  $c_p$  refer to boat speed, wind drift, current velocity (including

the effect of orbital motion<sup>10)</sup> and the speed of the scattering object on the water surface, respectively. Note that equation (1) is approximate since the vertical surface motion is ignored. The plus and minus signs refer to approaching or receding contributions, respectively. If the speed of the scattering object is associated with the underlying water wave then  $c_p$  is the phase speed of the water wave given by

$$c_p = \sqrt{\frac{g}{k_w} + \frac{\gamma}{\rho} k_w}, \quad (2)$$

where  $g$  is the gravitational acceleration,  $\gamma$  and  $\rho$  are the water surface tension and density, respectively, and  $k_w$  is the associated wavenumber. For Bragg scattering,

$$k_w = k_B \equiv \frac{4\pi \cos \theta_g}{\lambda} \quad (3)$$

is the Bragg-resonant wavenumber in water. Research has shown that a good approximation to the wind drift is 4% of the wind speed, a value we will use.<sup>11</sup>

The data considered here consist of against wind, cross wind and circle runs. During the runs, surface truth data were simultaneously collected using the diagnostics mentioned in the surface truth sensor package. Data gathering runs were conducted at boat speeds in the range of 0.9–1.4 m/s. The wind speeds at 10 m above the water surface were in the range of 5–13.5 m/s for the data presented.

## 4. Results

### 4.1 Grazing angle dependence of time-averaged Doppler spectra

#### 4.1.1 Against-wind runs

The term, against-wind run, refers to a data-collection run during which the scatterometer is looking against the propagation direction of the dominant wave. Examination of the one-minute time-averaged Doppler spectra for against-wind runs for grazing angles between 10° and 70° reveals that, at large grazing angles, the HH profile is similar to the VV profile, both peaking at more or less the same frequencies. However, the HH profile is sensitive to the grazing angle. *As the grazing angle is decreased, the peak of the HH spectrum gradually shifts toward higher Doppler frequencies, thus causing a*



separation of the HH peak from the VV peak. A few examples are shown to illustrate this point. In Figure 3, the Doppler spectra for both HH and VV returns are quite similar at large grazing angle ( $\theta_g = 55^\circ$ ) where two prominent peaks are clearly visible: a peak at 70 Hz (corresponding to a slower scatterer speed<sup>12</sup> of 83.3 cm/s) and a sharper, smaller peak at 100 Hz (corresponding to a faster speed of 168.3 cm/s) which will be designated as "slow" and "fast" peaks, respectively. As the grazing angle is reduced to  $\theta_g = 25^\circ$  (Fig. 4), although the "slow" peak is still dominant in the VV return, the "fast" peak is slightly larger (a few dB in spectral density) than the "slow" peak in the HH return, in other words, we have recorded peak shifting (the shift from the "slow" to the "fast" peak) in transition. At a grazing angle of  $\theta_g = 10^\circ$  (Fig. 5), peak separation<sup>13</sup> has occurred. The fast peak has become the dominant peak of the HH Doppler profile and only several gentle "wrinkles" remain in the profile at the frequency location of the "slow" peak. Finally, for RSRE data<sup>14</sup> at  $\theta_g = 6^\circ$  (Fig. 6), we see complete peak separation. Note that the HH profile is completely dominated by the "fast" peak without any hint that a slow component is present. This is typical of Doppler profiles seen at very low grazing angles.

We see then that peak separation is more accurately understood as a *gradual* relinquishing of dominance by the "slow" peak of the HH spectra with decreasing grazing angle. We will refer to the grazing angle at which dominance in the HH spectrum is transferred as the "switch-over" angle. We find that for wind speeds of 5–13.5 m/s, switch-over occurs at grazing angles between 25° to 15°. The switch-over angle is probably also wind-speed and sea-state dependent. Since these data were gathered at sea and not obtained under *controlled* laboratory conditions, a more precise value of the "switch-over" grazing angle is not available at this time.

At each grazing angle, the Doppler frequency at the "slow" peak corresponds reasonably well to that given by equation 1, with  $c_p$  matching the phase speed of the Bragg-resonant water-wave. The "fast" peak, however, corresponds to scatterers which move in the water reference frame at speeds much faster than the Bragg wave speed. As an example, the "fast" peak in Figure 5 corresponds to a speed which is about 100 cm/s faster than the speed corresponding to the "slow" peak. We shall comment further on this point later.

#### 4.1.2 Cross-wind runs

A cross-wind run means that the scatterometer is looking perpendicular to the propagation direction of the dominant wave. While prominent "fast" peaks were present in the Doppler spectra for against-wind runs, they were *absent* in the cross-wind runs for all

grazing angles between  $10^\circ$  and  $70^\circ$ . For cross-wind viewing directions, peak separation does not occur for low grazing angles, i.e., both the VV and HH spectra peak at more or less the same frequency. An example is shown in Figure 7, for  $\theta_g = 25^\circ$ . Compare this with Figure 4 and note the obvious absence of the “fast” peak. To first order, the observed Doppler frequency in the cross-wind case corresponds quite well to the boat velocity. Closer scrutiny, however, reveals that the peak may be slightly upshifted or downshifted from the “reference frequency” (i.e., Doppler frequency corresponding to boat speed only) depending on whether approaching or receding Bragg waves, respectively, were dominant in contributing to the backscatter return. If both approaching and receding Bragg wave contributions were equal, then an appropriate broadening of the Doppler spectrum about the “reference frequency” is observed.

For the most part, cross-wind viewing angles provide results which can be adequately described by Bragg scattering. However, in a few isolated cases, for Doppler spectra averaged over short times (a few seconds), we do observe Doppler peaks located exactly at the “reference frequency”, but with a Doppler bandwidth *sufficiently narrow* that the scattering appears to be the reflection from a body of “still” water (i.e., zero scatterer speed in the boat direction) rather than from patches of Bragg resonant waves, thus indicating the possibility of non-Bragg scattering.

#### 4.2 Time-dependent VV and HH signals

In order to further study the slow and fast scatterers, we examine the slow and fast contributions separately. The VV and HH scatterometer signals were band-pass filtered (with a filter width of  $\sim 10-15$  Hz) at frequencies centered about the Doppler frequency of the “slow” and “fast” peak values obtained from the time-integrated Doppler spectra (Figs. 3-6) for the entire length of the return record. These records were nominally 120s long for our data and 50s for RSRE data. Henceforth, we will refer to these filtered Bragg and faster-than-Bragg signals simply as *Slow* and *Fast* signals, respectively. A few short examples are shown only to indicate the characteristic features.

##### 4.2.1 Slow (i.e., Bragg) signals

The general features for Slow return-loss signals are found in *both* against-wind and cross-wind runs. In Figures 8 and 9, 12-second records of the Slow signal for an against-wind run, are shown for  $\theta_g = 10^\circ$  and  $30^\circ$ . In the figures, the lowest trace represents HH(t), the middle trace VV(t), and the top trace the polarization ratio HH(t)/VV(t), all in units of dB. Comparing the characteristic features as a function of

grazing angle, we note that as the grazing angle increases, the temporal correlation ("synchronization") between HH and VV signals improves. On the average, the HH signal appears to be comparatively spikier at smaller grazing angles. This spikiness is more pronounced in the total (unfiltered) signals an example of unfiltered signals at  $\theta_g = 10^\circ$  is shown in Fig. 14. The polarization ratio fluctuates about some mean value, but *never* exceeds 0dB, i.e., HH(t) is *always smaller* than VV(t).

#### 4.2.2 Fast (i.e., faster-than-Bragg) signals

Since no Fast peaks are found in the cross-wind runs, band-passed Fast signal data include only against-wind runs. In Figures 10 and 11, 12-second records of the return loss Fast signal, for against-wind runs, are shown for  $\theta_g = 10^\circ$  and  $35^\circ$ . In the figures, the lowest trace represents HH(t), the middle trace VV(t), and the top trace the polarization ratio HH(t)/VV(t), all in units of dB. The improvement in temporal "synchronization" of HH and VV signals with increasing grazing angle is again noted. The polarization ratio fluctuates about some mean value, the fluctuation being more vigorous than that seen in the polarization ratio of Slow signals. Most notable is the fact that the polarization ratio sometimes *equals or exceeds* 0dB, i.e., *there are instances where  $HH(t) \geq VV(t)$* . We call such instances "super" events, since HH equals or surpasses VV. Such occurrences are not confined to small grazing angles, "*super*" events occur for all grazing angles. Data on the probability of occurrence of  $HH \geq VV$  events per unit antenna illumination area (i.e., footprint area) will be presented in Section 6.

#### 4.3 Grazing angle dependence of polarization ratio

##### 4.3.1 Slow (i.e., Bragg) signals

The time-averaged polarization ratio (HH/VV) of band-passed Slow signals versus grazing angle is shown in Figure 12. The mean value is plotted as the data point while the standard deviation within the record is plotted as the error bar (one  $\sigma$  above and one  $\sigma$  below the data point). The scatter for RSRE data-points reflects the evaluated data for 256 range cells. For smaller grazing angles, our polarization ratio data are plotted against the effective (i.e., median) grazing angle.<sup>15</sup> The effective grazing angle is a necessary correction since the antenna pattern has finite beamwidth. No such correction is made for the RSRE data since a range-resolving radar in conjunction with a  $1^\circ$ -beamwidth antenna was used for the measurement. The gradual decrease in HH/VV with decrease of grazing angle is expected. Note that the cross-wind data (squares) and the against-wind data (circles) are in very good agreement.

### 4.3.2 Fast (i.e., faster-than-Bragg) signals

The Fast HH(t)/VV(t) signals are also averaged over the whole record. The mean value is plotted against the grazing angle, and the standard deviation is plotted as the error bar. The scatter for RSRE data-points again reflects the evaluated data for 256 range cells. The results are shown in Figure 13. The same effective grazing angle corrections were used to plot these data. The polarization ratios for Fast signals appear to be *insensitive* to grazing angle and have values between -3 dB to -10 dB, with an average value of  $-7.45\text{ dB}$  and a standard deviation of  $\pm 1.86\text{ dB}$ .

## 5. Comparison with theory

### 5.1 Slow (i.e., Bragg) signals

Peake<sup>16</sup> used the first-order fields from Rice's theory<sup>17</sup> to obtain backscattered power for vertical and horizontal polarizations. The average backscatter cross-section per unit area of the ocean, of horizontal and vertical polarizations from a slightly rough dielectric surface, for an incident plane wave polarized horizontally and vertically, respectively, given by Valenzuela<sup>18</sup>, are

$$\sigma_{o(HH)} = 16\pi k_m^4 \sin^4 \theta_g \left| \frac{(\epsilon - 1)}{(\sin \theta_g + \sqrt{\epsilon - \cos^2 \theta_g})^2} \right|^2 W(k_B, 0), \quad (4)$$

and

$$\sigma_{o(VV)} = 16\pi k_m^4 \sin^4 \theta_g \left| \frac{(\epsilon - 1)[\epsilon(\cos^2 \theta_g + 1) - \cos^2 \theta_g]}{(\epsilon \sin \theta_g + \sqrt{\epsilon - \cos^2 \theta_g})^2} \right|^2 W(k_B, 0), \quad (5)$$

where  $k_m = 2\pi/\lambda$  is the microwave wavenumber,  $\epsilon$  is the *complex* relative dielectric constant,  $W$  is the two-dimensional wave-amplitude power spectral density (PSD) of the surface and  $k_B$  is the Bragg-resonant wavenumber for surface waves.

Using the Debye equation<sup>19</sup> for the complex relative dielectric constant of a polar liquid in the microwave band, we calculated the dielectric constant of the sea water corresponding to actual temperature and salinity conditions at Loch Linnhe and the Sound

of Sleat.<sup>20</sup> For a microwave frequency of  $9.3\text{GHz}$  appropriate to our scatterometer, we obtain

$$\epsilon = 51.4 - i39.1 \quad (6)$$

Our calculated relative dielectric constant differs from the oft-quoted and oft-used values of  $\epsilon = 65 - i40$  and  $\epsilon = 65 - i30.7$ . The former value is from Saxton<sup>21</sup> for  $f = 10\text{GHz}$  and a water temperature of  $20^\circ\text{C}$ , while the latter value is from Kerr<sup>22</sup> for  $\lambda = 3.2\text{cm}$  and a water temperature of  $28^\circ\text{C}$ . Both of these sets of values are inappropriate for our experimental conditions.

Using equation 6 for the dielectric constant, the theoretical polarization ratio (using equations 4 and 5) is evaluated and plotted as a function of grazing angle in Figure 12. Also plotted for comparison is the polarization ratio for a perfect conductor, a model sometimes favored for simplicity<sup>23</sup> but clearly inappropriate as evidenced by the poor agreement with the data. Notice that Rice's theory fits the experimental data down to a grazing angle of  $\sim 20^\circ$  when the appropriate dielectric constant is used. At grazing angles less than  $\sim 20^\circ$ , Rice's theory begins to deviate from the experimental data. We suggest several arguments to account for the deviation:

- 1) During the absolute calibration of our scatterometer, we obtained cross section measurements from geometrical objects using spheres and cylinders. A sphere is a *degenerate* scatterer in the sense that it *does not* differentiate between polarizations, whereas a cylinder is a *non-degenerate* scatterer in the sense that it *does* differentiate between polarizations. A degenerate object scatters microwaves isotropically while a non-degenerate object scatters microwaves non-isotropically. In the process of using backscattered power measurements from cylindrical targets of diminishing radii to establish the polarization-isolation limit of our scatterometer system, we established that an alignment inaccuracy can also impose a limit on the achievable polarization isolation. The limit, for the case that the fields of both transmitted polarizations are equal in magnitude, is given by :

$$\left(\frac{HH}{VV}\right)_{\text{limit}} = 10 \log(\tan^4 \delta) \quad (7)$$

where  $\delta$  is the limiting angular alignment accuracy between the vertically-polarized electric field vector and the axis of a cylinder. If we *conjecture* that a misalignment of a non-degenerate target is limiting the polarization ratio, then a relative *roll* of the

scattering surface (as opposed to pitch, or *tilt* in microwave-scattering jargon, which changes the local grazing angle) with respect to the scatterometer could impose a lower limit on the polarization ratio. However, if the  $-20\text{ dB}$  measured polarization ratio at an effective grazing angle of  $13^\circ$  represented a lower limit, it would correspond to a combination of boat and scattering-surface rolling at a relative angle of  $\delta \approx 17^\circ$ . This value is an order of magnitude too large compared to the actual relative roll of the boat and surface. Thus boat rolling can *not* be an effective mechanism. On the other hand, if we adopt the two-scale Bragg model, then surface tilt could be a possible mechanism, but not at large grazing angles since positive and negative tilt contributions would cancel. At very small grazing angles, however, Bragg patches on negatively tilted surfaces would be shadowed, resulting in an increase in the measured polarization ratio due to the positive tilting of Bragg patches. At  $13^\circ$ , the contribution of positive tilt to the polarization ratio is  $0.81\text{ dB/degree}$ , thus a positive surface tilt of  $6.2^\circ$  could account for the measured polarization ratio.

- 2) There is another clue which may provide deeper insight. We mentioned earlier the observation that the temporal correlation of the Slow HH(t) and VV(t) signals deteriorates with decreasing grazing angle. This result suggests that at low grazing angles, either the vertical and horizontal polarizations are sometimes obtaining returns from *different* patches of water,<sup>24</sup> i.e., different locations in the “nominal” illumination spot, or are seeing returns from the *same* patch but with a polarization-ratio value in disagreement with the prescription provided by Rice's theory. Both these situations are possible *if*: i) there is preferential diffraction of the vertical polarization into the shadow region (the back side of a dominant wave) *or* ii) multipath scattering occurs. If either case were true, then  $W(k_b, 0)$  would *not* be common to both HH and VV (see Equations 4 and 5). While Rice's theory would still be correct, the usage in that form, i.e., assuming  $W(k_b, 0)$  to be common to both polarizations for *all* times, would be inappropriate. Alternatively, if Brewster reflection is involved in the multipath scattering process, Rice's theory can still be used provided that VV is multiplied by the appropriate attenuation factor due to Brewster reflection. Although it is questionable whether multiple scattering will prove significant in influencing backscattering microwave returns from an ocean surface, it is mentioned as a possibility.

In any case, it is evident that for grazing angles smaller than  $\sim 20^\circ$ , Rice's theory cannot explain the Slow signal data without recourse to additional mechanisms.

## 5.2 Fast (i.e., faster-than-Bragg) signals

To explain the Fast signals, concepts previously introduced, such as two-scatterer models, scattering from breaking waves or returns from the tips-of-dominant-waves<sup>25-28</sup> seem to be slowly gaining acceptance. It is uncertain if any useful theory, with either predictive or postdictive capability, is available at the moment. However, vigorous effort toward construction of a realistic theory is in progress.<sup>29</sup> It is certain, from review of the data presented so far, that there are other scattering mechanisms besides Rice's mechanism.<sup>30</sup> To summarize, we have the following experimental results from the Fast signals: 1) After accounting for the wind drift, platform speed, orbital motion etc., the Doppler frequency of the Fast signal corresponds to a velocity which *far exceeds* the Bragg-resonant wave phase speed. 2) The *time-averaged* polarization ratio of the Fast signal is roughly constant, ranging between  $-3\text{dB}$  to  $-10\text{dB}$ , and is insensitive to grazing angle. 3) The *time-resolved* polarization ratio  $\text{HH}(t)/\text{VV}(t)$  of the Fast signal can *occasionally* equal or exceed unity. Each of these results is in violent disagreement with Rice's theory.

What mechanisms may give rise to the observed data? The first result points to returns from scatterers associated with a faster wave, that is, a water wave of much longer wavelength than the Bragg-resonant wave. The second result points to possible returns from wave-breaking (incipient or otherwise) of the longer waves and from "specular facets"<sup>31</sup> associated with the longer wave. The third result points to *either* non-degenerate objects whose orientations favor the horizontal polarization return, *or* multipath scattering in which one reflection occurs at the Brewster angle so that the vertical polarization return is substantially attenuated. It should be stressed, however, that most of the time, VV is observed to dominate over HH. Before embarking on further discussion of this issue, more data are presented in the following section to support the above conjectures.

## 6. Additional data and discussion

### 6.1 Time-resolved Doppler spectra

Of the many sequences of time-resolved Doppler spectra available in our data that strongly support the mechanisms which we have suggested as giving rise to the Fast signals, we offer one example. Figure 14 shows a 12-second portion of a total (i.e., not band-passed filtered) temporal record of the return-loss signal at  $\theta_g = 10^\circ$ . The bottom trace represents  $\text{HH}(t)$ , the middle trace  $\text{VV}(t)$ , and the top trace  $\text{HH}(t)/\text{VV}(t)$ . As noted

earlier, the HH returns are "spikier" at low grazing angles and this is again obvious from the figure.

Eight frames of Doppler spectra taken from the record (Fig. 14), from  $t = 16.6s$  to  $t = 18.0s$  at  $200ms$  intervals, are shown in Figure 15. The Slow ( $f_S$ ) and Fast ( $f_F$ ) Doppler frequencies, obtained from the time-integrated Doppler spectrum (Fig. 5), are marked by arrows. The light curve is the VV spectrum and the dark curve is the HH spectrum. At time  $t = 16.6s$ , the Fast part of the spectrum has no energy. In the next two frames,  $t = 16.8s$  and  $17.0s$ , spectral energy contributions from fast scatterers are evident. Notice that in the Fast portion of the spectrum at  $t = 16.8s$ ,  $HH \sim VV$ ; at  $t = 17.0s$ ,  $HH > VV$ , and at  $t = 17.2s$ ,  $VV \gg HH$ . At time  $t = 17.0s$  and later frames, notice how the spectral density at the Fast frequency "cascades" down toward the Slow frequency, thus filling in the spectrum of frequencies between  $f_F$  and  $f_S$ . Again, at  $t = 17.6s$ ,  $HH \gg VV$ , followed by  $HH \sim VV$  ( $t = 17.8s$ ), then  $HH < VV$  ( $t = 18.0s$ ), and again accompanied by a cascade of energy from  $f_F$  to  $f_S$ .

The various features observed in the eight frames of Doppler spectra in Figure 15 may represent the scatterometer returns from an incipient wave-breaking or micro-breaking process. A possible hydrodynamic scenario is sketched out in Figure 16. At time step 1, the scatterometer sees free Bragg waves and the Doppler frequency corresponds to the Bragg wave phase speed. At time step 2, breaking is just about to occur on the forward face of the fast wave. This could form a degenerate scatterer which does not distinguish polarization, or it could form a non-degenerate scatterer which favors either the VV or HH polarization. However, the Doppler frequency will correspond to the phase speed of the fast wave. At post-breaking times, steps 3, 4 and 5, a bore may form, or by-products of the "broken" wave (foam, bubbles, shorter waves) may be "trapped" temporarily at the crest vicinity of the fast wave and eventually be *shed* by the fast wave and left behind. This results in a variety of scatterers which at first exhibit the fast wave phase speed but eventually decelerate to the free Bragg-wave phase speed, if they are able to survive the transition. Thus one should observe the "cascading" of the Fast Doppler frequency to *intermediate frequencies*, and finally to the Slow Doppler frequency. Although the actual data do not have an exactly one-to-one correspondence with the steps in the idealized scenario, the main features described above can be seen in the sequence of time-resolved Doppler spectra.



## 6.2 Wind-direction dependence of Doppler spectra

The against-wind and cross-wind spectral data have already underscored the fact that ocean backscatter is *not* isotropic. This is easy to understand since waves propagate and also break, predominantly in the wind direction. For the cross-wind look, the scatterometer does not see (or very seldom sees) breaking waves and therefore does not show a prominent Fast component in the Doppler spectra.

An additional set of data in support of our arguments as to the identification of scattering mechanisms is presented in Figure 17. This set was obtained by running the boat in a clockwise circle in the same wind-wave field. The boresight grazing angle of the scatterometer was fixed at  $\theta_g = 35^\circ$ .

The Doppler spectra are 20-second averages, with boat headings taken at  $45^\circ$  intervals with respect to the wind direction. Starting from  $\phi = 0^\circ$  or  $360^\circ$  (top spectrum in the Figure) the Slow peak is at  $\sim 75\text{ Hz}$  ( $49\text{ cm/s}$ ), the Fast peak is at  $\sim 125\text{ Hz}$  ( $145\text{ cm/s}$ ). Notice that the Slow peak is dominant for the HH spectrum since the grazing angle used is larger than the "switch-over" angle. Looking clockwise in the figure, one sees the  $\phi = 45^\circ$  case where both port- and head-wind components are present, both the Slow and Fast components are still present but the Fast component is diminished in power. In the cross wind case ( $\phi = 90^\circ$ ) in which only the Slow component is evident, the Fast spectral components at  $\sim 110\text{--}140\text{ Hz}$  have practically *disappeared* ( $40\text{ dB}$  lower compared to the  $0^\circ$  case). The cases between  $\phi = 135^\circ$  to  $225^\circ$  all have stern-wind components as well as fast waves propagating *away* from the scatterometer, therefore the spectra contain scattering from receding elements and are thus shifted to lower frequencies. In the case in which the boat is running *with* the wind ( $\phi = 180^\circ$ , bottom spectrum), there is partial blocking of the fast waves as well as the wind by the boat, and the scatterometer sees predominantly randomly-distributed Bragg waves. The peak at around  $-20\text{ Hz}$  could be due to scattering from parts of a *receding* long wave of  $1.8\text{ m}$  wavelength, or from an unidentified object, maybe a water fowl, that was flying away at  $1.68\text{ m/s}$ . Another cross-wind case is encountered at  $\phi = 270^\circ$  where Fast components are absent. The case at  $\phi = 315^\circ$  again has a head-wind component and with it the re-appearance of Fast components in the Doppler spectra. It should be pointed out that the Doppler spectra are short time averages and the boat speed as well as the wind speed varied somewhat during the course of the circle run (as seen from simultaneous recordings of the temporal wind speed and boat speed), therefore one should not expect the Doppler spectra of the two cross-wind (port- and starboard-wind) runs to be *exactly* identical. The same general

features were verified in another circle run (this time, counter-clockwise) in a different wind-wave field and at a smaller grazing angle, but we refrain from showing the data in the interest of brevity.

The circle-run data thus further substantiate the several suggested backscattering mechanisms from wind-wave surfaces. To summarize, the mechanisms are: 1) Bragg scattering, at all angles relative to the wind and at all grazing angles, contributes to the Slow peak in the Doppler spectrum, with polarization ratios in accordance with Rice's theory (modifications are required, however, at low grazing angles). 2) Scattering from the wave crest vicinity (from micro- or macro-breaking events) provides energy at the Fast peak and energy between Fast and Slow peaks (i.e., the "cascade" frequencies) in the Doppler spectrum for against-wind look directions at all grazing angles. 3) Preferential diffraction of vertical polarization into the shadow region, and multipath scattering represent possible mechanisms to explain the decorrelation of the VV and HH signals (by the former mechanism) and the deviation of the polarization ratio from Rice's theory (by the latter mechanism) at low grazing angles for Slow and Fast signals. 4) Scatterometer returns determined both by the specific orientation of non-degenerate scatterers with respect to microwave fields, and possible multiple (multipath) scattering events which include a reflection at the Brewster angle,<sup>32</sup> can provide the polarization ratio associated with "super" events.

### 6.3 Probability of "super" events

Returning to the topic of "super" events mentioned earlier in Section 4.2.2, recall that the definition refers to instances when  $HH(t) \geq VV(t)$  and occurs only for Fast signals. Strict adherence to Rice's theory would render such a result impossible since according to this theory, HH should always be less than VV, unless at normal incidence (i.e.,  $90^\circ$  grazing angle) where backscatter theoretically becomes independent of polarization.<sup>33</sup> However, if one accepts the notion that there exist non-degenerate scattering objects which are capable of preferentially scattering horizontally polarized radiation, then "super" events are natural. To find out *how* natural they are, we quantify "super" events by providing a measure of their occurrence.

In Figure 10, at time  $t = 27.5s$ , one observes a "super" event which lasts for roughly 0.2 seconds. Similarly, such events are seen at  $t = 27.8s$ ,  $28.5s$ ,  $30.5s$ , and so on throughout the record. For time-resolved band-passed Fast signals at each grazing angle, we *sum the duration* of all such "super" event occurrences ( $\Sigma \Delta t$ ), then divide this time by the total length of the record ( $T$ ) and by the illumination area  $A_{FP}$  (i.e., the antenna

footprint area, defined by the  $-3dB$  beamwidth of the radiation pattern) to obtain the probability of occurrence of “super” events per unit antenna footprint area

$$P = \frac{\Sigma \Delta t}{T A_{FP}} \quad (8)$$

Figure 18 shows  $P$  plotted as a function of grazing angle ( $P$  has dimensions of  $m^{-2}$ ). The solid points are our data and the hollow points are RSRE data. We find an approximate exponential dependence of  $P$  with respect to grazing angle, giving

$$P = \frac{1}{B} \exp\left(\frac{\theta_g}{\theta_o}\right) \quad (9)$$

with parameters  $B = 2 \times 10^3 m^2$  and  $\theta_o = 14.89^\circ$  providing the best fit. The triangular data point does not fit on the curve. However, if we look up the wind record for this particular run, we find that the wind speed ( $5 m/s$ ) is the lowest of all the runs. This would indicate that the probability of occurrence of super events may be a function of sea state and thus of wind speed and fetch.

For large grazing angles, it should be obvious that the probability of scattering from specular facets (whether degenerate or non-degenerate) will be much higher than at low grazing angles simply because the distribution of water surface slopes strongly favors the smaller slopes. This can be a partial explanation for the data in Figure 18. The results also indicate that in the range of wind speeds between  $5-13.5 m/s$  for which these data were obtained, “super” events are rather rare (i.e.,  $VV > HH$  most of the time). However, the occurrence of “super” events at low grazing angles is sufficient to raise the *time-averaged* polarization ratio to values which greatly exceed the values prescribed by Rice's theory, thus lending support to the conjecture that the scattering is from objects other than grating-like patches of Bragg waves. Since Bragg scattering provides very little return of horizontally polarized radiation for low grazing angles, “super” events can be important and in fact become the dominant contributor to the returns for horizontal polarization, in spite of their low probability of occurrence.

#### 6.4 Comparison of backscattering cross-sections

In order to compare Bragg scattering cross-sections with cross-sections due to non-Bragg mechanisms (e.g., specular facets), we provide a simplified estimation by comparing the cross-sections per unit of area of ocean from *pure* specular reflection with the Bragg scattering for, say, horizontal polarization. By *pure* specular reflection, it is *assumed*, for the sake of argument, that the return is from a large *flat* surface of water with surface normal in the direction of the boresight grazing angle. We have

$$\frac{\sigma_{PURE\ SPECULAR}}{\sigma_{BRAGG\ SCATTER\ (HH)}} \sim \frac{\sin \theta_g |R_F|^2}{\sigma_{o(HH)}}, \quad (10)$$

where  $R_F$  is the Fresnel reflection coefficient for normal incidence (i.e.,  $90^\circ$  grazing angle)

$$R_F = \frac{\sqrt{\epsilon} - 1}{\sqrt{\epsilon} + 1} \quad (11)$$

with  $\epsilon$  being the computed relative dielectric constant given by equation (6).  $\sigma_{o(HH)}$  is given by equation (4). To evaluate equation (10), we need to know the value of the product of the fourth power of the microwave wavenumber and the Bragg-resonant 2-D wave-height PSD, i.e.,  $k_m^4 W(k_B, 0)$ . Comprehensive two-dimensional wave-height power spectral density data were obtained from surface slope data measured during the experiment using our scanning laser slope gauge.<sup>8,34</sup> Our data show that values of  $W(k_B, 0)$  are dependent on wind-speed and wind-direction, with the grazing angle dependence being implicit in the Bragg wavenumber. As an example, for a wind speed of  $10.9\text{ m/s}$ , at grazing angle of  $10^\circ$  and for an against-wind direction, our measurement yields

$$k_m^4 W(k_B(\theta_g), 0) \approx 4.8 \times 10^{-5}. \quad (12)$$

Inserting the appropriate values into equation (10), we find that at  $10^\circ$  grazing angle, the *pure* specular reflection cross-section is larger than the horizontally-polarized Bragg scattering cross-section by a factor of  $\sim 8 \times 10^4$ . In other words, in an antenna footprint of say,  $50\text{ m}^2$ , a  $6\text{ cm}^2$  purely specular area would provide the same backscattered power as the horizontally-polarized Bragg return from the entire footprint. Generally, however, non-Bragg cross-sections are expected to be smaller than *pure* specular cross-sections, a *pure*

reflector model is used in this example only to provide an *upper limit* for the estimation of non-Bragg scattering cross-sections. In principle, the cross-section due to any non-Bragg scattering mechanism could be calculated if the size, shape and orientation of the particular scattering object were known. The present example serves to illustrate that only a *small* fraction of the antenna footprint area is required for non-Bragg scattering mechanisms to provide a non-negligible return. The fraction can be anywhere in the range of  $10^{-2} - 10^{-5}$ , depending on the facet geometry as well as the wind speed, wind direction, microwave polarization and grazing angle.

### 6.5 Coherence properties of scatterers

The coherence properties of scatterers in the antenna footprint of a CW scatterometer can provide clues to the nature of the scattering processes. The study of the problem, however, is complicated by the fact that 1) there are different types of scattering mechanisms (e.g., Bragg and specular-like), 2) there is a distribution of the size of the scatterers, 3) the scatterers can have different lifetimes, and 4) there can be a distribution of scatterer speeds. Nevertheless, we will attempt to gain some insight by examining two *idealized* cases which we will use as simple models.

The normalized autocorrelation function of the backscattered field is given by

$$\gamma_{ii}(\tau) = \frac{\langle E_i^*(t)E_i(t+\tau) \rangle}{\langle E_i^*(t)E(t) \rangle}, \quad (13)$$

where  $E(t)$  and  $E^*(t)$  are the complex amplitude and its complex conjugate, respectively, or simply the I and Q signals of the backscattered field;  $\tau$  is the lag time; the subscript  $i$  refers to either vertical or horizontal polarization and angular brackets denote temporal average. We examine the following two special cases.

#### *Case 1: Lifetime-dominated scattering*

Assume that all scatterers (patches or facets) are of the same size and are moving at the same speed, then the scattered field from the  $n^{\text{th}}$  scatterer can be expressed as

$$E_n(t) = E e^{(i\omega_n + i\theta_n)t} e^{-\frac{t}{2\tau_c}}, \quad (14)$$

where  $\omega_o$  is the scattered frequency,  $\theta_n$  is the phase which is assumed to be random, and  $\tau_e$  is the average lifetime of the scatterer (i.e., the one e-folding time of the backscattered power). The normalized autocorrelation function, using equation (13), is thus

$$\gamma_{ii}(\tau) = e^{i\omega_o\tau} e^{-\frac{|\tau|}{2\tau_e}}. \quad (15)$$

The absolute value of  $\gamma_{ii}$  will yield an exponential-decay behavior with respect to the lag time.

*Case 2: Scattering dominated by scatterers with Gaussian distribution of speeds*

Assume that the scatterers are of the same size but the scatterer lifetimes are sufficiently long that the process is *not* lifetime dominated. Assume that the scatterers are moving at *different* speeds, the distribution of which is assumed to be Gaussian. For this case, the scattered intensity (i.e., the power spectral density, or the Doppler spectrum) is given by

$$P(\omega) = \frac{1}{\sqrt{\pi}\omega_E} e^{-\frac{(\omega-\omega_o)^2}{\omega_E^2}}, \quad (16)$$

where  $\omega_o$  is the center frequency (e.g., the peak of the Doppler spectrum) and  $\omega_E$  is the halfwidth at the one e-folding point in the spectrum. Since the autocorrelation function is the Fourier transform of the power spectral density

$$G(\tau) = \int_{-\infty}^{\infty} P(\omega) e^{i\omega\tau} d\omega, \quad (17)$$

it is straightforward to compute the normalized autocorrelation function by noting that

$$\gamma_{ii}(\tau) = \frac{G(\tau)}{G(0)}. \quad (18)$$

Using expressions (16) to (18), one obtains

$$\gamma_{ii}(\tau) = e^{i\omega_o\tau} e^{-\left(\frac{\tau}{2\tau_e}\right)^2}, \quad \text{where } \tau_e \equiv \omega_E^{-1}, \quad (19)$$

so that the absolute value of  $\gamma_{ii}$  is Gaussian with respect to lag time.

Comparing equations (15) and (19), one notes that the shapes of the normalized autocorrelation function for the two cases are entirely different. Also, the slopes at zero lag time are different: for Case 1,  $d|\gamma|/d\tau = -0.5\tau_e^{-1}$ ; while for Case 2,  $d|\gamma|/d\tau = 0$ .

A model based on the two special cases predicts that at large grazing angles, Bragg scattering dominates over scattering from fast events for both polarizations; the returns should therefore be characterized mainly by the spread in scatterer velocity, thus the shape of the normalized autocorrelation function for both polarizations should be similar. At small grazing angles, in addition to Bragg scattering, the returns are also strongly influenced by scattering from fast events (probably from wave crests of longer waves) which occur sporadically in time. The scattering can thus be “lifetime dominated” as well. Since the horizontal polarization will be affected more than the vertical polarization, the normalized autocorrelation function should therefore be narrower in width and exhibit more of an exponential decay for the horizontal than for the vertical polarization. Two examples of our data are shown. In Figure 19, for an against-wind look at  $10^\circ$  grazing angle, we see that  $\gamma_{HH}(\tau)$  is narrower than  $\gamma_{VV}(\tau)$ , with a one e-folding time of  $\sim 25ms$  (average facet lifetime) for the horizontal polarization. Examination of recorded video images of the footprint reveal micro-wavebreaking events which can sometimes be observed in one frame and not in the next frame. Since video images are obtained at  $30Hz$  (the interframe time is  $33ms$ ), this result indicates that a facet lifetime of  $\sim 25ms$  is not unrealistic. When model exponential and Gaussian curves are fitted through the one e-folding point of the  $\gamma_{VV}(\tau)$  (or  $\gamma_{HH}(\tau)$ ) data, we find that the normalized autocorrelation function is bracketed *between* these model limits. In Figure 20, for an against-wind look at  $55^\circ$  grazing angle, the normalized autocorrelation functions for both polarizations are almost identical, with  $\gamma_{HH}(\tau)$  being slightly narrower than  $\gamma_{VV}(\tau)$ . Model curve fits through the one e-folding points verify that the normalized autocorrelation functions are truly Gaussian-like, thus the halfwidth at half-maximum value of  $\sim 0.05s$  corresponds to a  $-3dB$  Doppler bandwidth of  $\sim 6.5Hz$ .

In general, we have the following observations: for cross wind cases at large grazing angles where there is very little contribution from fast scatterers, the normalized autocorrelation functions for both polarizations are practically identical and are also Gaussian in shape. For smaller grazing angles at both against-wind and cross-wind configurations,  $\gamma_{HH}$  is usually narrower than  $\gamma_{VV}$ , i.e.,  $\gamma_{HH}$  decorrelates faster than  $\gamma_{VV}$ ,

and both curves lie between the exponential and Gaussian limits, indicating that scattering from the crest region of a breaking wave is playing a major role. Finally, the *quantitative* difference between the normalized autocorrelation functions obtained for the two opposite types of configurations are shown in Figure 21 for the vertical polarization (the horizontal polarization data are similar but not shown). For the small-grazing-angle against-wind case,  $\gamma_{VV}(\tau)$  is bracketed between the exponential and the Gaussian model curves, while for the large-grazing-angle cross-wind case,  $\gamma_{VV}(\tau)$  is practically Gaussian except for a small deviation at lag times beyond the one e-folding point.

It is interesting to note that this simple model is able to correctly describe certain gross features of the physical process. A word of caution, however, is necessary. The simple model should not be stretched too far since all the factors mentioned in the first paragraph of this section are expected to play a role. In reality, the processes and the coherence properties of scatterers are quite complex.

## 6.6 Spiking

“Spiking” (sometimes also called a “burst”) has become a topic of some interest in recent years. It has been described as a radar scattering event at grazing angles *less than*  $10^\circ$  associated with scattering caused by the crest of a steep or breaking fast wave and it is distinguished by its long decorrelation time (i.e., rare occurrence) and very large values of HH/VV.<sup>35</sup>

We find in our data ample evidence to suggest that the term “spiking” requires a broader, and at the same time, clearer definition. There are instances when spiking is observed even in the *Slow* signal, for example: in Figure 8, spiking occurs in the HH signal (at  $t = 12.5s$ ,  $13.4s$  and  $17.2s$ ), however, since  $HH < VV$ , we find that “spiking” does not necessarily produce a “super” event; also, since it *is* a *Slow* signal (the Doppler frequency corresponds to a Bragg wave), it can *not* be associated with a breaking faster-than-Bragg wave. On the other hand, in cases where  $HH > VV$ , we find that “super” events are not necessarily due to “spiking”, e.g., see Fig. 11, at  $t = 37.2s$ . Furthermore, “super” events are *by no means* restricted to grazing angles smaller than  $10^\circ$ . We also observe “negative spiking”, e.g., in Fig. 10, at time  $t = 33.2s$ , VV increases upwards while HH spikes *downwards*, yielding, for that particular moment, a very small polarization ratio ( $-20dB$ ) which deviates greatly, by  $-15dB$ , from the average value (see Fig. 13 for the average value).



Having cited examples of so-called “spiking” in our ocean wave data which fall outside the narrow definition of the term, we thus ask: What is spiking? What average decorrelation time between spikes is required? How short should the burst be? How far should the spiking power deviate from some time-averaged value? Lacking a general consensus regarding the definition of a spike or burst, it appears, for the moment, that “spiking” is in the eye of the beholder.

In the narrow sense of the definition of “spiking” described in the first paragraph in this section, we think that it is simply a hydrodynamically-created surface condition which resulted in some non-degenerate object (flotsam, jetsam, water fowl, flying fish and seal heads excluded) which favored the horizontal polarization return, yielding  $HH > VV$ . In a slightly broader sense, a “burst” is defined as the specular reflection from a very large water surface ( $kd \gg 1$ ) yielding  $HH = VV$ . Wave breaking is of course a prime candidate for “horizontal events”, sometimes also called “line events”, popular for its capability of explaining  $HH > VV$  data. There are several constraints, however, on the positive identification of a simple “horizontal” scattering object: 1) the measured polarization ratio defines the possible “aspect ratio” (length/width) of the object, 2) the measured backscattered power defines the effective radar cross section which, taken with point 1), must define a physically realistic shape,<sup>36</sup> and finally, 3) the Doppler frequency provides the information on whether the object is moving at the speed of a fast wave or otherwise. A similar set of constraints exist on the positive identification of a pure specular reflector (for case  $HH = VV$ ). Thus, simple models are readily testable for physical reality when invoked to explain scattering sources or objects. We suspect that in general, spiking (in the broad sense) is due to complex shapes and could also be a complicated mixture of several mechanisms.

## 7. Summary

We have performed an ocean experiment of microwave backscattering for a large range of grazing angles ( $10^\circ$  to  $70^\circ$ ), thereby obtaining grazing-angle-dependent results. This has enabled us to make the connection between large and small grazing angle backscattering data and thus distinguish between Bragg and faster-than-Bragg components, resulting in a clear identification of different types of scattering sources. With this distinction made, we could elucidate additional features, such as “super” events that are due to the faster-than-Bragg waves, and happen *not only* for small grazing angles, but for *all* grazing angles. By analyzing time-resolved and wind-direction dependent Doppler spectra, we could verify the compelling presence of mechanisms additional to Bragg

scattering. We were able to quantify "super" events and proposed that hydrodynamic processes could *occasionally* produce non-degenerate fast scatterers to yield HH equal to or greater than VV. We were also able to see that Bragg scattering is still operative for the horizontal polarization at small grazing angles, albeit overshadowed by the faster-than-Bragg events, so that Rice's theory need not be abandoned too hastily. By examination of the coherence properties of the backscattered signals, we were also able to see that the autocorrelation functions at low grazing angles are clearly distinct for different polarizations, thus providing strong evidence for the presence of lifetime-dominated, non-Bragg scattering events. Finally, we have found sufficient examples to demonstrate that "spiking" is in dire need of a clearer definition.

We find our results to be in good agreement with certain aspects of past ocean experiments,<sup>1-6</sup> and our present suggestions of scattering mechanisms also echo past conjectures.<sup>25-28</sup> However, our experiments and synoptic view provide clarification, extensions and an integration of many past suggestions.

We suggest that the unsolved problem of low-grazing-angle scattering should be approached by formulating a quantitative theory based on the contributions from the proposed scattering features, i.e., Bragg waves, breaking waves, non-degenerate "facets", etc. Of course, not all scattering objects will have to be included in order to account for the predominant backscatter characteristics. The difficulty of incorporating the physics of a breaking wave while retaining Rice's model in a quantitative theory is considerable and it is easy to understand why currently available theories (e.g., composite theory, higher order expansions, etc.) are inadequate. However, we hope that the present set of results will provide the necessary experimental evidence to prompt substantial improvements to the present scattering theories.

#### **Acknowledgment**

This work was conducted under the auspices of Office of Under Secretary of Defense / Naval Warfare and Mobility, under contract with Lawrence Livermore National Laboratory (Subcontract B157282).

## References

1. Goldstein, H., "Sea echo" in *Propagation of Short Radio Waves* (D.E. Kerr, Editor), Dover Reprint, originally publ. M.I.T. Radiation Laboratory Series Vol. **13** (1947).
2. Pidgeon, V.W., "Doppler dependence of radar sea return", *J. Geophys. Res.* **73**, 1333 (1968).
3. Mel'nichuk, Yu. V., and A.A. Chernikov, "Spectra of radar signals from sea surfaces for different polarizations", *Izv. Atmos. & Oceanic Phys.* **7**, 28 (1971).
4. Long, M.W., "On a two-scatter theory of sea echo", *IEEE Trans. Antennas & Propagation* **AP-22**, 667 (1974).
5. Leykin, A.I., I.Ye. Ostrovskiy, A.D. Rozenberg, V.G. Ruskevich, and I.M. Fuks, "The effect of long waves on energy spectra of radar signals scattered from a sea surface", *IVUZ Radiofiz.* **3**, 346 (1975).
6. Kalmykov, A.I., and V.V. Putovoytenko, "On polarization features of radio signals scattered from the sea surface at small grazing angles", *J. Geophys. Res.* **81**, 1960 (1976).
7. Barter, J.D., K.L. Beach, C.L. Hindman, B.M. Lake, P.H.Y. Lee, H. Rungaldier, J.C. Shelton, R. Yee, "Calibration of the TRW X-band radar", TRW Report No. 58101-6001-UT-06, January, 1993. Redondo Beach, CA.
8. Lee, P.H.Y., J.D. Barter, K.L. Beach, C.L. Hindman, B.M. Lake, H. Rungaldier, J.C. Schatzman, J.C. Shelton, R.N. Wagner, A.B. Williams, R. Yee, H.C. Yuen, "Recent advances in ocean surface characterization by a scanning laser slope gauge", *SPIE Proc.* **1749**, 234 (1992).
9. Barter, J.D., K.L. Beach, B.M. Lake, P.H.Y. Lee, H. Rungaldier, J.C. Shelton, R.N. Wagner, "Catalog and summary of TRW data from the Joint UK/US West Coast Experiment, Scotland, 1991", TRW Report No. 58101-6001-UT-01, Sept. 1991. Redondo Beach, CA.
10. Lee, P.H.Y., "Doppler measurements of the effects of gravity waves on wind-generated ripples", *J. Fluid Mech.* **81**, 225 (1977).

11. Lange, P., and H. Hühnerfuss, "Drift response of monolayer slicks to wave and wind action", *J. Phys. Oceanography* **8**, 142 (1978).
12. The scatterer speed refers to the component of the scatterer velocity parallel to the boat heading in the water frame of reference. It contains the phase speed of the scattering wave as well as the wind drift and current contributions. This is *not* the relative radial velocity in the direction of the scatterometer boresight which contains the boat velocity.
13. Peak separation refers to the separation of the HH spectral peak from the VV spectral peak in the Doppler spectra. See reference 2 for one of the earliest documentations of this phenomenon observed at low grazing angles.
14. This and subsequent RSRE data at grazing angle  $\theta_g = 6^\circ$  were obtained in 1989 at Loch Linnhe, Scotland. Data kindly provided by Dr. K. Ward of DRA-Malvern, U.K..
15. The effective grazing angle is calculated by convolving the  $R^{-4}$  range dependence with the measured antenna pattern and the illuminated area (i.e., footprint); under the assumption that scatterers are uniformly distributed, it represents the median, since half the return power comes from local grazing angles larger than the median, while the other half comes from local grazing angles smaller than the median. The correction is non-negligible for small boresight grazing angles and negligible for large boresight grazing angles, e.g., the effective angle is  $13.1^\circ$  for a boresight angle of  $10^\circ$  while the effective angle is  $31.5^\circ$  for a boresight angle of  $30^\circ$ .
16. Peake, W.H., "Theory of radar return from terrain", *IRE Nat'l. Conv. Rec.* **7**, Pt. 1, 21 (1959).
17. Rice, S.O., "Reflection of electromagnetic waves from slightly rough surfaces", *Comm. Pure & Appl. Math.* **4**, 351 (1951).
18. Valenzuela, G.R., "Scattering of electromagnetic waves from the ocean", in *Surveillance of Environmental Pollution and Resources by Electromagnetic Waves* (T. Lund, Ed.) pp. 196-226, Reidel Publ. Co., Dordrecht, Holland (1978).
19. Debye, P., "*Polar Molecules*", Dover reprint, originally pub. Rheinhold Publ. Corp. (1929).

20. The dielectric constant is computed using  $\epsilon = \epsilon' - i\epsilon''$ , with real and imaginary parts of the dielectric constant given by

$$\epsilon' = \frac{\epsilon_s - \epsilon_o}{1 + (\omega\tau)^2} + \epsilon_o \quad \text{and} \quad \epsilon'' = \frac{\omega\tau}{1 + (\omega\tau)^2}(\epsilon_s - \epsilon_o) + \frac{2\sigma_i}{f},$$

where  $\epsilon_s$  is the static permittivity,  $\epsilon_o$  is the dielectric constant representing the sum of electronic *and* atomic polarizations,  $\omega = 2\pi f$  is the radial microwave frequency,  $\tau$  is the characteristic dipole relaxation time of the polar molecule and  $\sigma_i$ , the ionic conductivity, is the *additional* term to the Debye equation for sea water. For conditions appropriate to Loch Linnhe and the Sound of Sleat (temperature:  $10^\circ - 12^\circ C$ , and salinity:  $28 - 34 ISU$ ), we obtain from extant data [Saxton, J.A., and J.A. Lane, "Electrical properties of sea water", *Wireless Engineer* **29**, 269 (1952)]:  $\epsilon_s = 74$ ,  $\epsilon_o = 4.9$ ,  $\tau = 12.2 ps$  and  $\sigma_i = 0.31 \times 10^{11}$  (*e.s.u. units*).

21. Saxton, J.A., "Electrical properties of water: reflection characteristics of water surfaces of V.H.F.", *Wireless Engineer* **26**, 288 (1949).
22. Kerr, D.E., W.T. Fishback and H. Goldstein, "Reflection from the earth's surface" in *Propagation of Short Radio Waves* (D.E. Kerr, Editor), Dover Reprint, originally publ. M.I.T. Radiation Laboratory Series Vol. 13 (1947).
23. For a perfect conductor, i.e., for the imaginary part of the dielectric constant tending towards infinity, the polarization ratio becomes a simple expression:

$$\lim_{\epsilon'' \rightarrow \infty} \frac{HH}{VV} = \left( \frac{\sin^2 \theta_g}{1 + \cos^2 \theta_g} \right)^2.$$

24. From our calibration of the antenna pattern, we find the -3 dB beamwidths of the horizontal and vertical polarizations are not exactly identical in the azimuthal and vertical planes. This means that the antenna footprint is not *exactly* identical for the horizontal and vertical polarizations. For example, at  $10^\circ$  grazing angle, the horizontal polarization sees ~18% more surface area in the azimuthal direction while the vertical polarization sees ~35% more area in the range direction. Due to the  $R^{-4}$  range dependence of scatterometer signals, the additional contribution to the polarization ratio is ~1 dB *if* scatterers were uniformly and isotropically distributed on the surface. Nevertheless, it is a fact that different polarizations will see different areas for *real* antennas at small grazing angles, which *may* account for the non-synchronization of HH and VV signals we observe in our data. Note that the difference in illumination spot size (between polarizations) along the range-direction

decreases when the grazing angle is increased. The difference in illumination spot size in the azimuthal-direction, however, remains independent of the grazing angle.

25. Long, M.W., "On a two-scatter theory of sea echo", *IEEE Trans. Antennas & Propagation* **AP-22**, 667 (1974).
26. Leykin, A.I., I. Ye. Ostrovskiy, A.D. Rozenberg, V.G. Ruskevich and I.M. Fuks, "The effect of long waves on energy spectra of radar signals scattered from a sea surface", *IVUZ Radiofiz.* **3**, 346 (1975).
27. Kalmykov, A.I., and V.V. Pustovoytenko, "On polarization features of radio signals scattered from the sea surface at small grazing angles", *J. Geophys. Res.* **81**, 1960 (1976).
28. Wetzel, L.B., "A model for sea backscatter intermittency at extreme grazing angles", *Radio Science* **12**, 749 (1977).
29. Caponi, E., B.M. Lake, P.H.Y. Lee, H.C. Yuen, "A hydrodynamic model for low-grazing-angle backscatter phenomena from the ocean", TRW Rep. No. 58101-6002-UT-00, August, 1993. Redondo Beach, CA.
30. For the sake of brevity, we will lump all the variations played upon Rice's theme (e.g., composite model) in *one* mechanism.
31. Microwave scattering from ocean waves is predominantly a diffractive process *even if* some scattering object has a local surface normal pointed at the scatterometer boresight. Specular reflection from a "specular facet" occurs when the facet has dimension  $d$  such that  $kd \gg 1$  ( $k$  is the microwave wavenumber). Therefore, scattering off a "specular facet" can yield either  $HH > VV$ , or  $HH = VV$ , or  $HH < VV$ , depending on the facet *size, shape* and *orientation*. Thus, *ray optics* should be used with caution in modeling since the most interesting effect, that of polarization, is *a priori* excluded. For the case where specular facets are considered in the context of explaining  $HH = VV$  results, see Kwoh, D.S., B.M. Lake, H. Rungaldier, "Microwave scattering from internal wave modulated surface waves: A shipboard real aperture coherent radar study in the Georgia Strait Experiment", *J. Geophys. Res.* **93**, 12235 (1988).
32. There is a low probability, however, of significant multiple scattering events which include a Brewster reflection, because the surfaces configuration has to be very special.

33. At normal incidence,  $HH = VV$  is true only in a time-integrated sense. Furthermore, the additional condition of either a glassy smooth surface or an isotropic distribution of scatterers (waves) is required. Neither condition is realistic for wind-wave surfaces since there are always dominant waves which travel in some preferred direction. The microwave polarization which is aligned with the wave crests will have a different return from the other (orthogonal) polarization. However, at angles approaching normal incidence, scattering from Bragg or faster-than-Bragg waves becomes unresolvable because the Doppler frequency (in the water-surface frame) tends to zero as the grazing angle tends to  $90^\circ$ , and only surface-elevation motion will be detected. Furthermore, at normal incidence, the Bragg resonance condition has a singularity.
34. Barter, J.D., K.L. Beach, C.L. Hindman, B.M. Lake, P.H.Y. Lee, H. Rungaldier, J.C. Schatzman, J.C. Shelton, R.N. Wagner, A.B. Williams, R. Yee, H.C. Yuen, "Slope gauge data products from Scotland 1991", TRW Rep. No. 58101-6001-UT-03, April, 1992, and "More slope gauge data products from Scotland 1991", TRW Rep No. 58101-6001-UT-04, August, 1992. Redondo Beach, CA.
35. See, e.g., Trizna, D.B., J.P. Hansen, P. Hwang and J. Wu, "Laboratory studies of radar sea spikes at low grazing angles", *J. Geophys. Res.* **96**, 12529 (1991), and references contained therein.
36. For example, a wave-surface area of  $0.05 \text{ m}^2$  with dimensions of  $2 \text{ mm}$  in width and  $25 \text{ m}$  in length, is hydrodynamically *unrealistic*.

## Figure captions

- FIG. 1 A schematic diagram of the dual-polarized, 8-channel X-band coherent scatterometer.
- FIG. 2 The calibrated two-way radiation pattern in the azimuthal plane.
- FIG 3 Time-integrated Doppler spectra of wind waves; against-wind look direction,  $\theta_g = 55^\circ$ . The VV trace has higher spectral density at both “slow” and “fast” peaks. The frequencies at the “slow” and “fast” peaks correspond to scatterer speeds (see definition in Ref. 10) of 83.3 cm/s and 168.3 cm/s, respectively.
- FIG. 4 Time-integrated Doppler spectra of wind waves, against-wind look direction,  $\theta_g = 25^\circ$ . The VV trace has higher spectral density at both “slow” and “fast” peaks. Peak separation of HH relative to VV is in progress (see text). The “slow” and “fast” peaks correspond to scatterer speeds of 33.4 cm/s and 126.7 cm/s, respectively.
- FIG. 5 Time-integrated Doppler spectra of wind waves, against-wind look direction,  $\theta_g = 10^\circ$ . The VV trace has higher spectral density at “slow” peak. Note that peak separation has occurred, HH has maximum spectral density shifted to “fast” peak. The “slow” and “fast” peaks correspond to scatterer speeds of 50 cm/s and 154 cm/s, respectively.
- FIG. 6 RSRE data from Loch Linnhe Experiment, 1989. Run #8, range cell 80. Time-integrated Doppler spectra of wind waves, against-wind look direction,  $\theta_g = 6^\circ$ . The VV trace has higher spectral density at the “slow” peak. Note that peak separation is complete, HH has maximum spectral density at the “fast” peak. The “slow” and “fast” peaks correspond to scatterer speeds of 41.9 cm/s and 133.2 cm/s, respectively.
- FIG. 7 Time-integrated Doppler spectra of wind waves; cross-wind look direction,  $\theta_g = 25^\circ$ . The VV trace has higher spectral density at “slow” peak. Compare with Figure 4 and notice the absence of a “fast” peak in both the VV and HH spectra.
- FIG. 8 A short sample of time-resolved, band-pass filtered Slow signals; against-wind look direction,  $\theta_g = 10^\circ$ . HH is the bottom trace, VV is the middle trace,



HH/VV (polarization ratio) is the top trace. Note that HH(t) and VV(t) are not well correlated in time. HH/VV *never* exceeds 0 dB.

FIG. 9 A short sample of time-resolved, band-pass filtered Slow signals; against-wind look direction,  $\theta_g = 30^\circ$ . HH is the bottom trace, VV is the middle trace, HH/VV is the top trace. Note that HH(t) and VV(t) are much better correlated in time and that HH/VV *never* exceeds 0 dB.

FIG. 10 A short sample of time-resolved, band-pass filtered Fast signals; against-wind look direction,  $\theta_g = 10^\circ$ . HH is the bottom trace, VV is the middle trace, HH/VV is the top trace. Note that HH(t) and VV(t) are not well correlated in time, but better correlated than the case in Figure 8. Note also that HH/VV *occasionally* equals or exceeds 0 dB. Also note that fluctuations of HH/VV about the mean value are larger than for the Slow case (Fig. 8).

FIG. 11 A short sample of time-resolved, band-pass filtered Fast signals; against-wind look direction,  $\theta_g = 35^\circ$ . HH is the bottom trace, VV is the middle trace, HH/VV is the top trace. Note that HH(t) and VV(t) are much better correlated in time. Note that HH/VV *occasionally* equals or exceeds 0 dB also for this intermediate grazing angle. As a matter of fact, for Fast signals, this occurs for *all* grazing angles (see text).

FIG. 12 Time-averaged polarization ratio of Slow signals. Solid circles are TRW against-wind runs, squares are TRW cross-wind runs, hollow circles are RSRE data. The error bar represents one standard deviation above and below the data point. The solid curve is Rice's theory with a dielectric constant appropriate for the water temperature and salinity of Loch Linnhe and the Sound of Sleat ( $\epsilon = 51.4 - i 39.1$ ). The poor agreement of Rice's theory using a *perfect conductor* model is indicated by the dotted curve.

FIG. 13 Time-averaged polarization ratio of Fast signals. Solid circles are TRW against-wind runs, hollow circles are RSRE data. Although there are some physics models, there is no theory, with predictive or postdictive capability, available for Fast signals at present.

FIG. 14 A 12-second sample record of the total signal for an against-wind run,  $\theta_g = 10^\circ$ . The lower trace is HH, the middle trace is VV and the top trace is HH/VV. Note that HH appears to be spikier. Between the time of 16.6 s to 18.0 s, eight frames of Doppler spectra will be shown in the following Figure.

- FIG. 15 A sequence of time-resolved Doppler spectra (the heavy curve is HH, the light curve is VV) depicting how horizontal and vertical polarizations occasionally indicate Fast returns. Note that in the Fast region, it is possible for HH to equal or exceed VV. Also note energy in “cascade” frequencies. Refer to text for description.
- FIG. 16 A possible scenario which can produce the type of Doppler spectra shown in Figure 15. The top picture is a depiction of the various stages of an incipient wave-breaking process. The evolution of the scatterer speed of the various types of scatterers is given in the bottom “phase velocity vs. time” graph.
- FIG. 17 Doppler spectra as a function of wind direction. This *circle-run* sequence was conducted at a fixed grazing angle of  $\theta_g = 35^\circ$ . Doppler spectra at  $45^\circ$  intervals with respect to the wind direction are shown. The data set starts and ends with the against-wind orientation ( $\varphi = 0^\circ$  and at  $\varphi = 360^\circ$ ). The HH spectrum can always be easily identified as having the lower spectral value at the peak frequency than the VV spectrum.
- FIG. 18 Probability of “super” events per unit footprint area as a function of grazing angle. Solid circles are TRW data, hollow circles are RSRE data. The triangle is a run at the lowest wind speed. The straight line is a least squares fit to the solid circles.
- FIG. 19 The normalized autocorrelation functions of the horizontal and vertical polarizations versus lag time. Against-wind look,  $\theta_g = 10^\circ$ . Note that  $|\gamma_{HH}|$  is more exponential-like while  $|\gamma_{VV}|$  is more Gaussian-like.
- FIG. 20 The normalized autocorrelation functions of the horizontal and vertical polarizations versus lag time. Against-wind look,  $\theta_g = 55^\circ$ . Both  $|\gamma_{HH}|$  and  $|\gamma_{VV}|$  are Gaussian-like and almost identical.
- FIG. 21 The quantitative difference between normalized autocorrelation functions for small-grazing-angle against-wind (upper graph) and large-grazing-angle cross-wind (lower graph) cases. The grazing angles are  $10^\circ$  and  $55^\circ$  for the upper and lower graphs, respectively. The solid line represents the experimental data, the *Gaussian model* is represented by the short dashed line while the *exponential model* is represented by the long dashed line. Note that for  $10^\circ$ ,  $|\gamma_{VV}|$  is bracketed between the two model curves, while at  $55^\circ$ ,  $|\gamma_{VV}|$  is practically Gaussian.

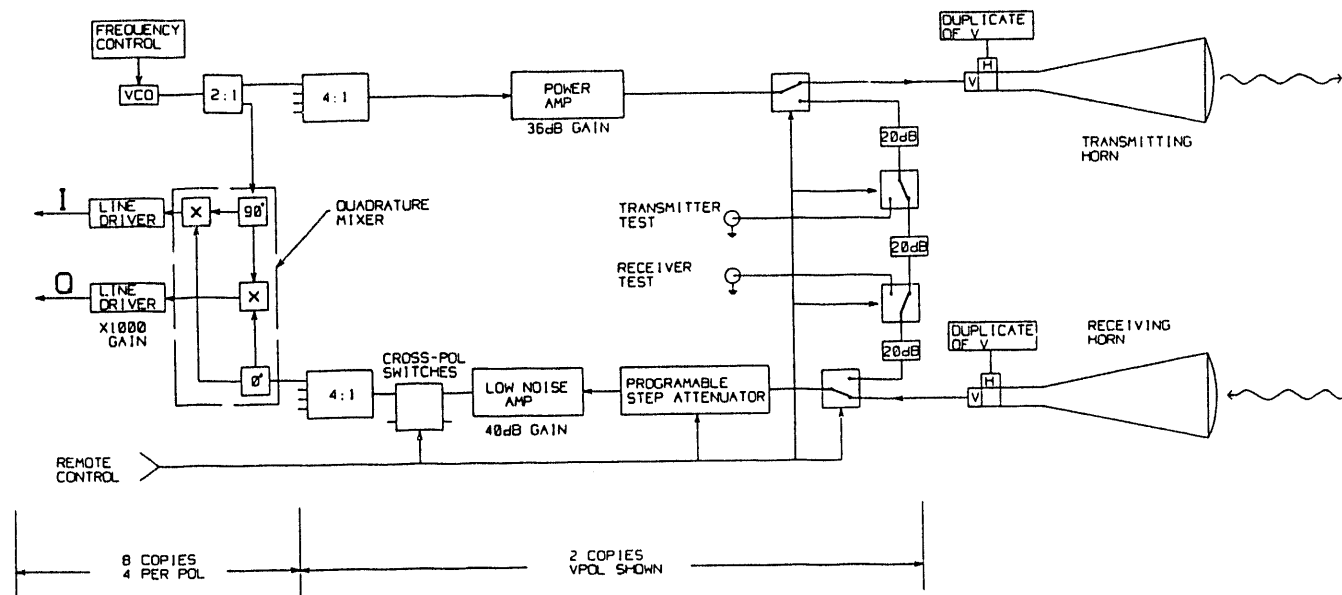


FIG. 1 A schematic diagram of the dual-polarized, 8-channel X-band coherent scatterometer.

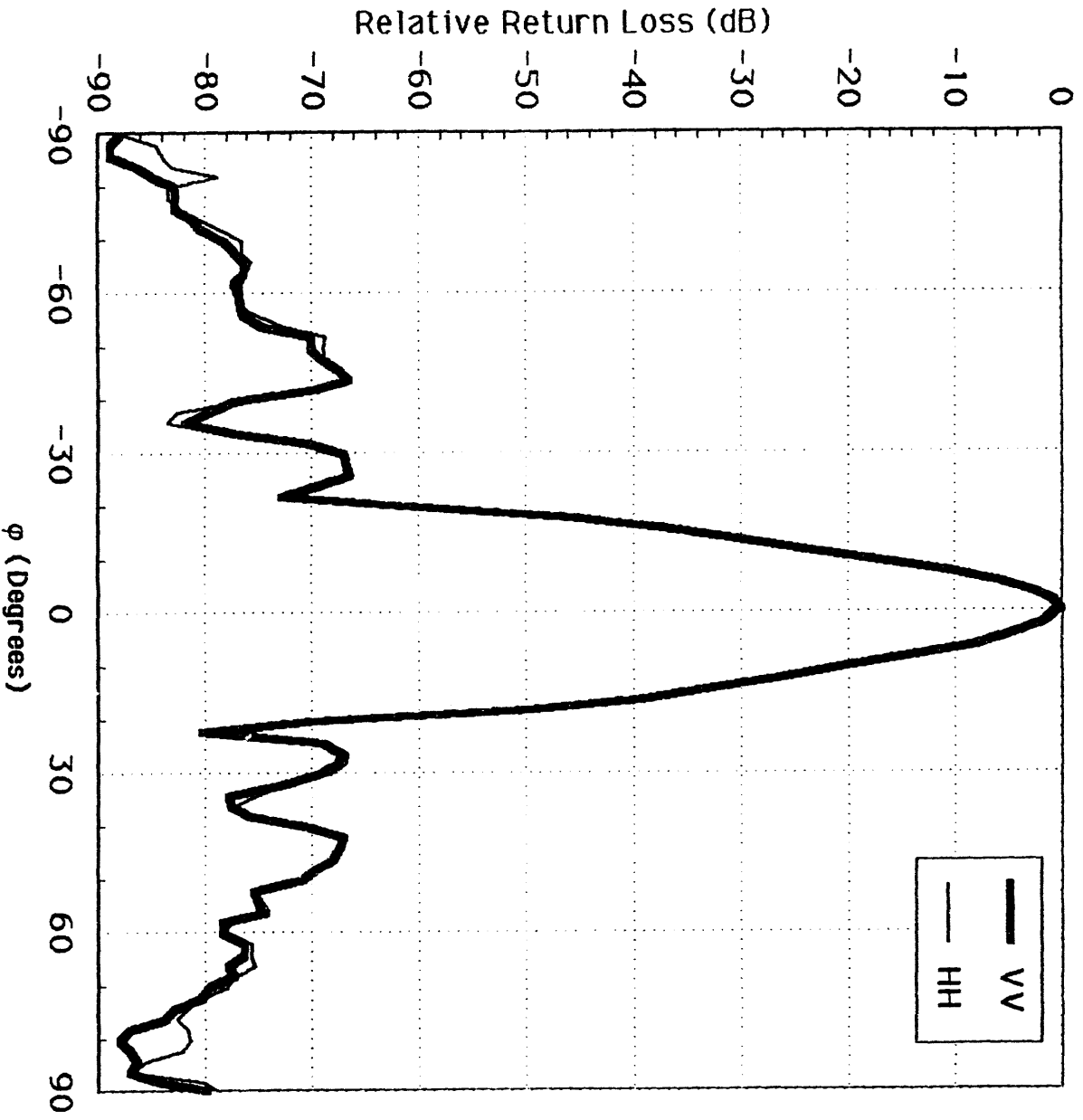


FIG. 2 The calibrated two-way radiation pattern in the azimuthal plane.

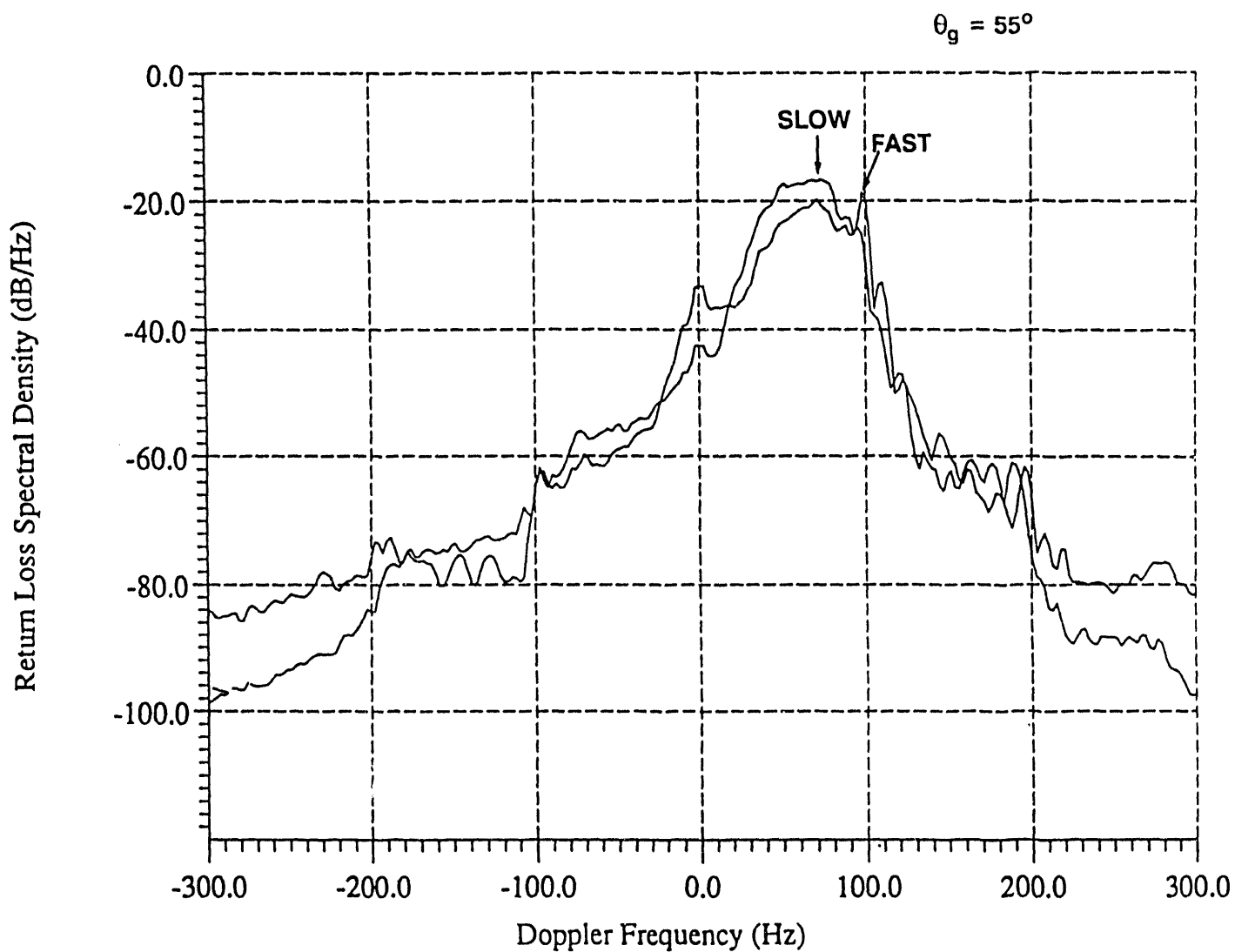


FIG.3 Time-integrated Doppler spectra of wind waves, against-wind look direction,  $\theta_g = 55^\circ$ . The VV trace has higher spectral density at both "slow" and "fast" peaks. The frequencies at the "slow" and "fast" peaks correspond to scatterer speeds (see definition in Ref. 10) of 83.3 cm/s and 168.3 cm/s, respectively.

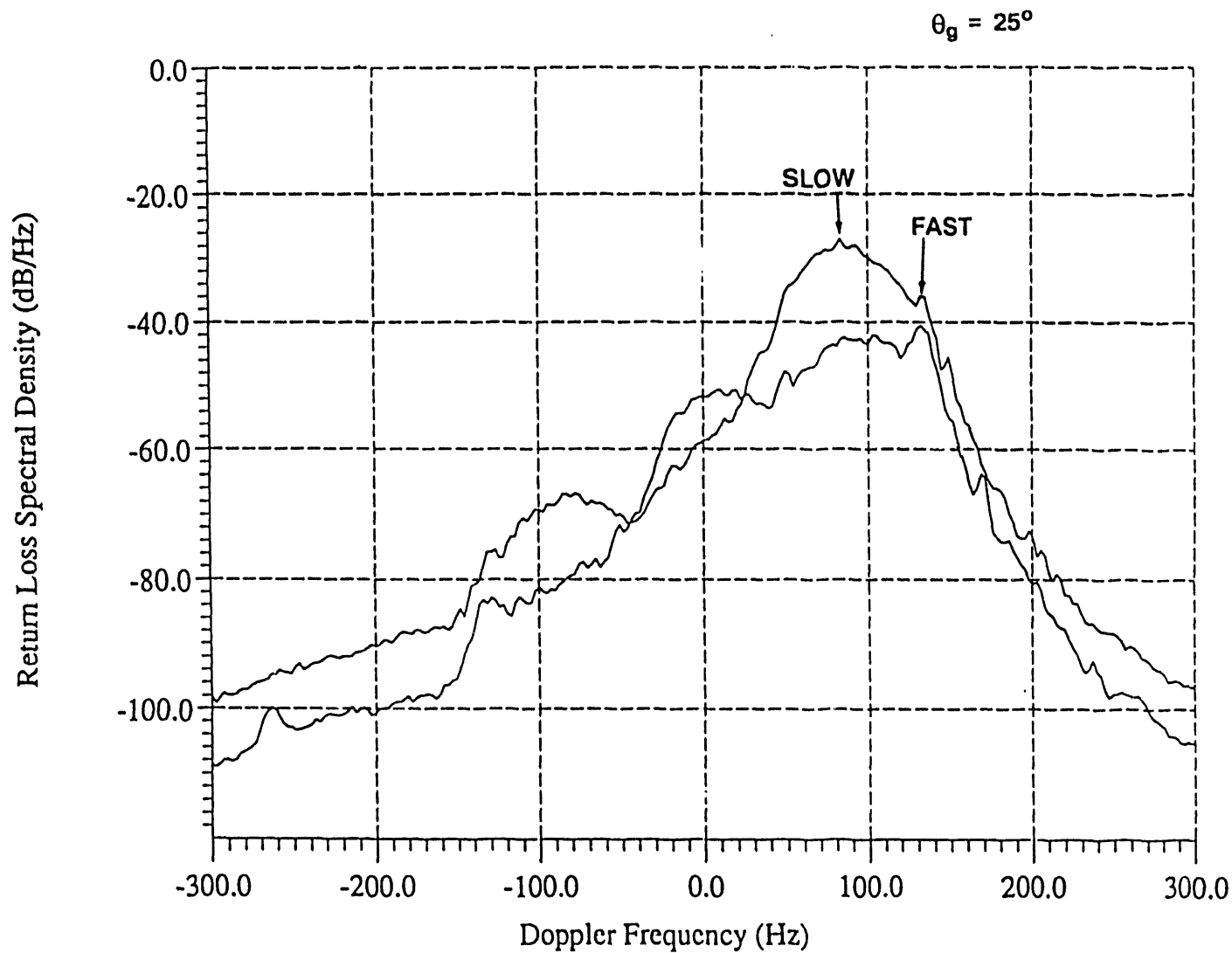


FIG. 4 Time-integrated Doppler spectra of wind waves, against-wind look direction,  $\theta_g = 25^\circ$ . The VV trace has higher spectral density at both "slow" and "fast" peaks. Peak separation of HH relative to VV is in progress (see text). The "slow" and "fast" peaks correspond to scatterer speeds of 33.4 cm/s and 126.7 cm/s, respectively.

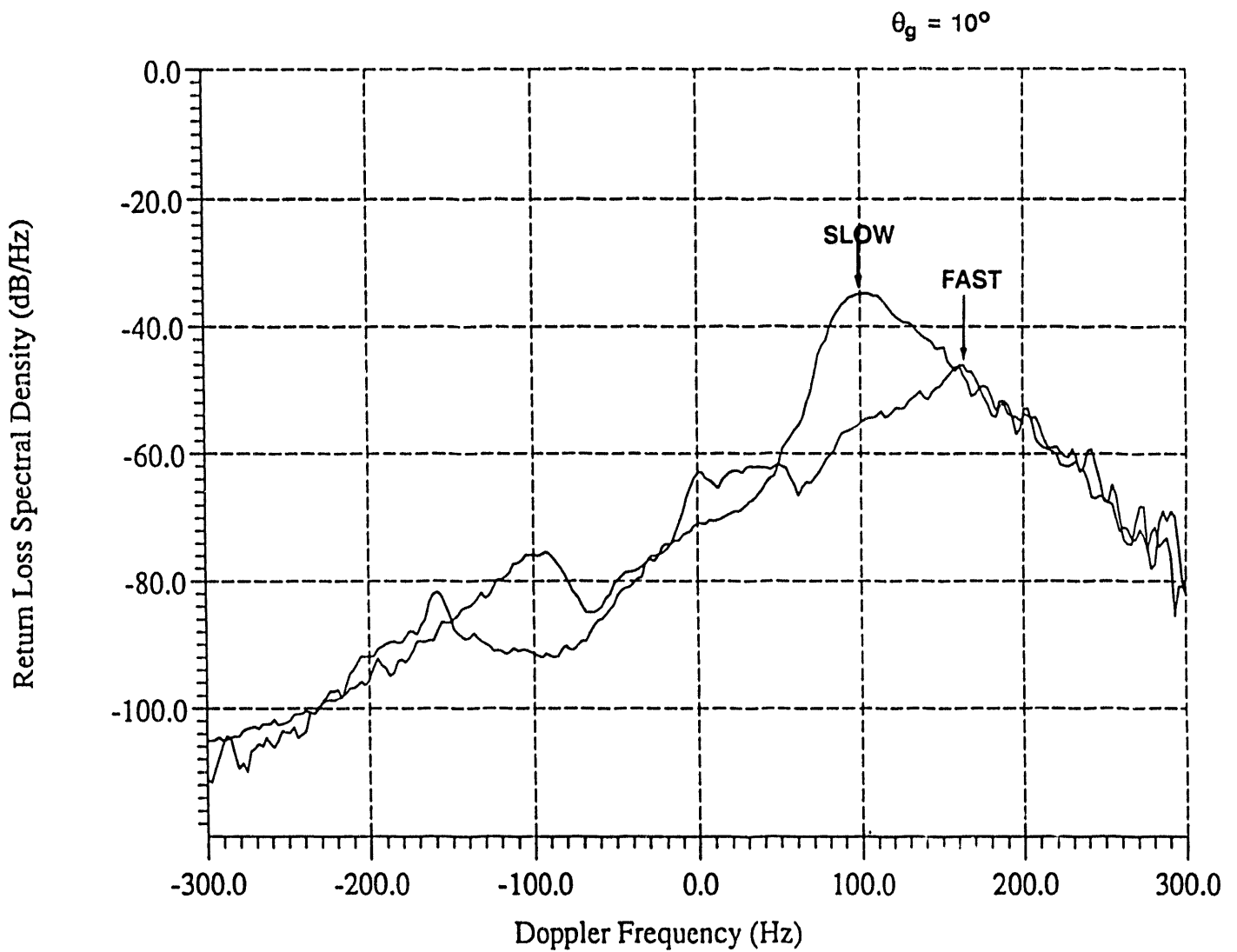


FIG. 5 Time-integrated Doppler spectra of wind waves, against-wind look direction,  $\theta_g = 10^\circ$ . The VV trace has higher spectral density at "slow" peak. Note that peak separation has occurred, HH has maximum spectral density shifted to "fast" peak. The "slow" and "fast" peaks correspond to scatterer speeds of 50 cm/s and 154 cm/s, respectively.

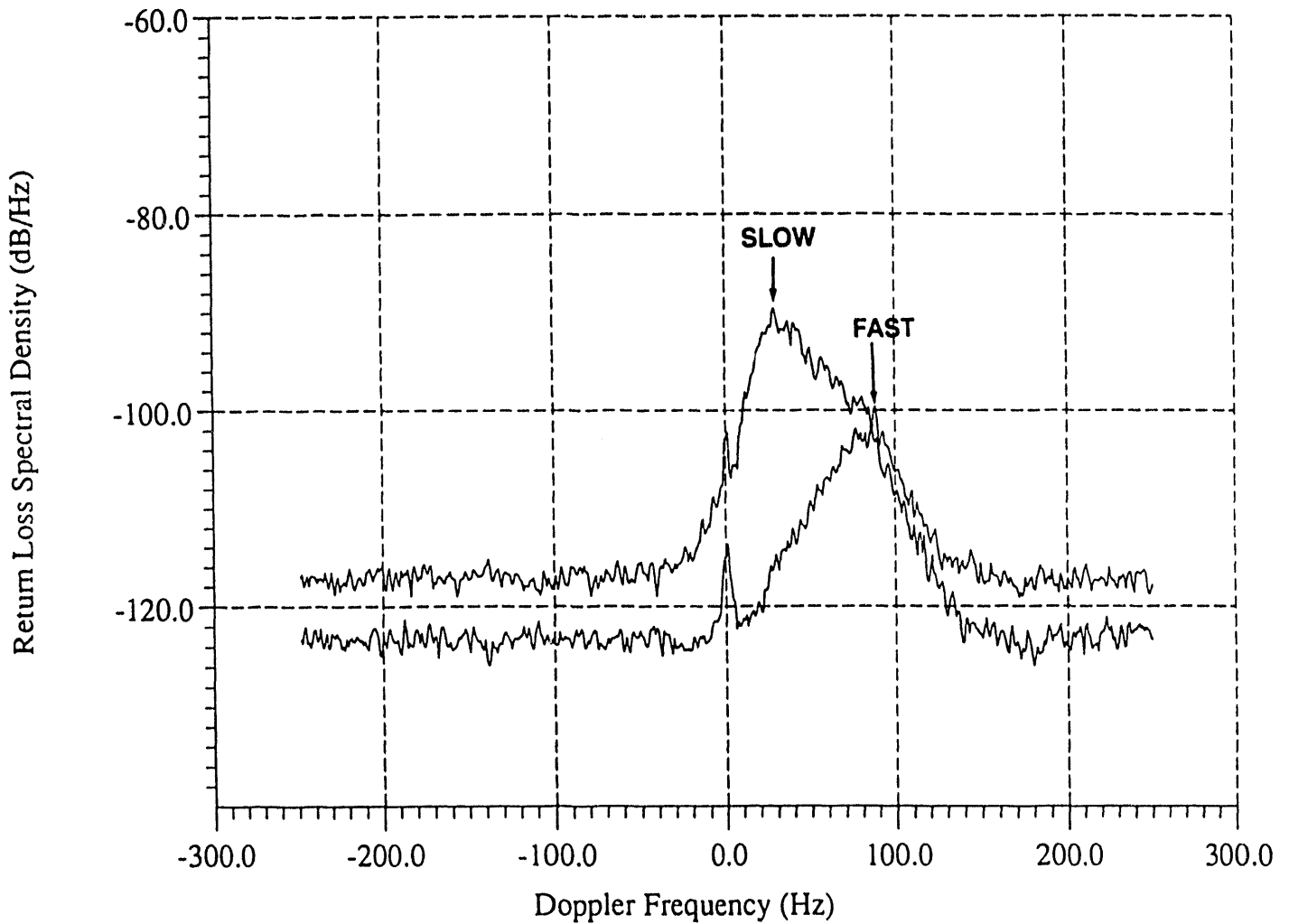


FIG. 6 RSRE data from Loch Linnhe Experiment, 1989. Run #8, range cell 80. Time-integrated Doppler spectra of wind waves, against-wind look direction,  $\theta_g = 6^\circ$ . The VV trace has higher spectral density at the "slow" peak. Note that peak separation is complete, HH has maximum spectral density at the "fast" peak. The "slow" and "fast" peaks correspond to scatterer speeds of 41.9 cm/s and 133.2 cm/s, respectively.



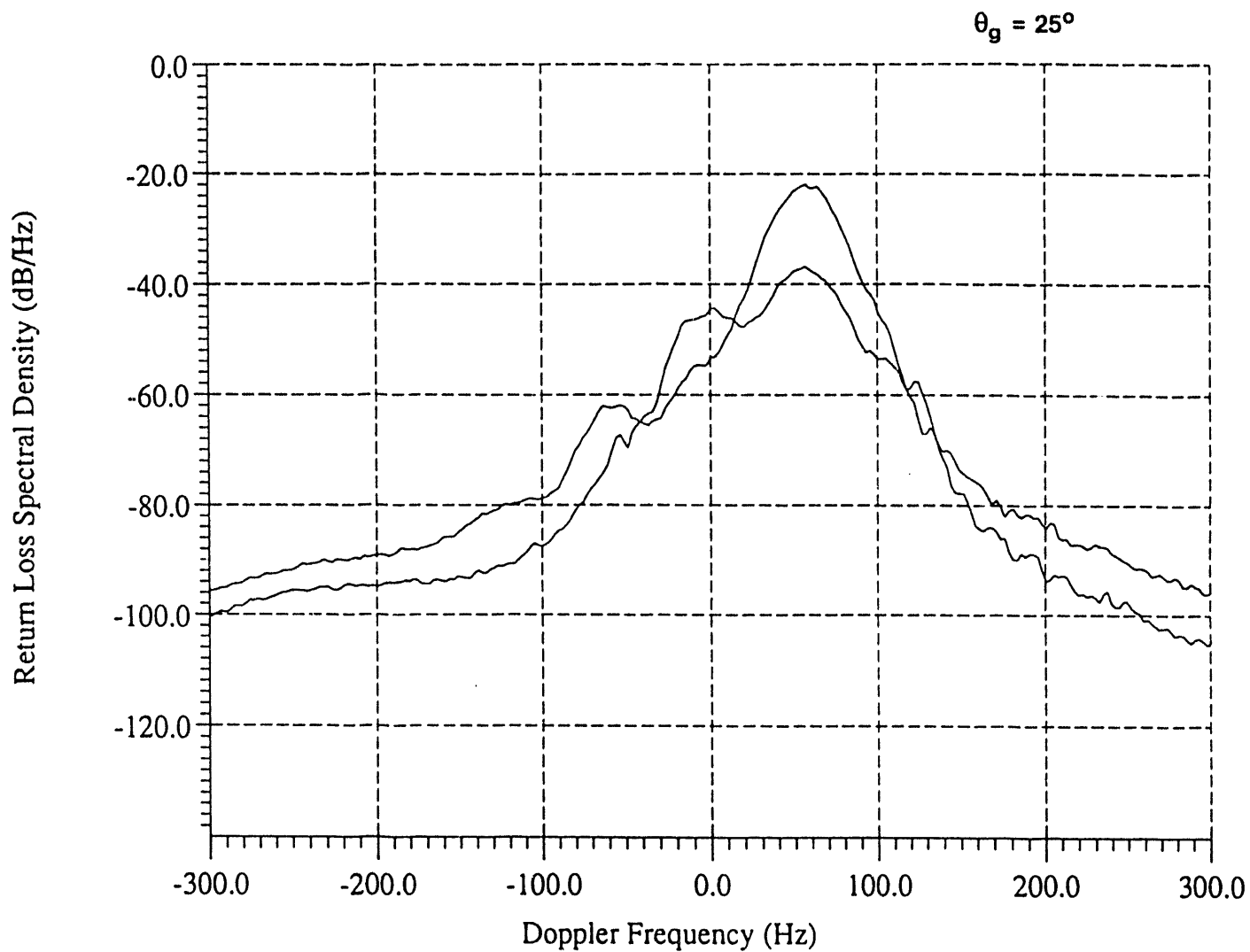


FIG. 7 Time-integrated Doppler spectra of wind waves, cross-wind look direction,  $\theta_g = 25^\circ$ . The VV trace has higher spectral density at "slow" peak. Compare with Fig. 4 and notice the absence of a "fast" peak in both the VV and HH spectra.

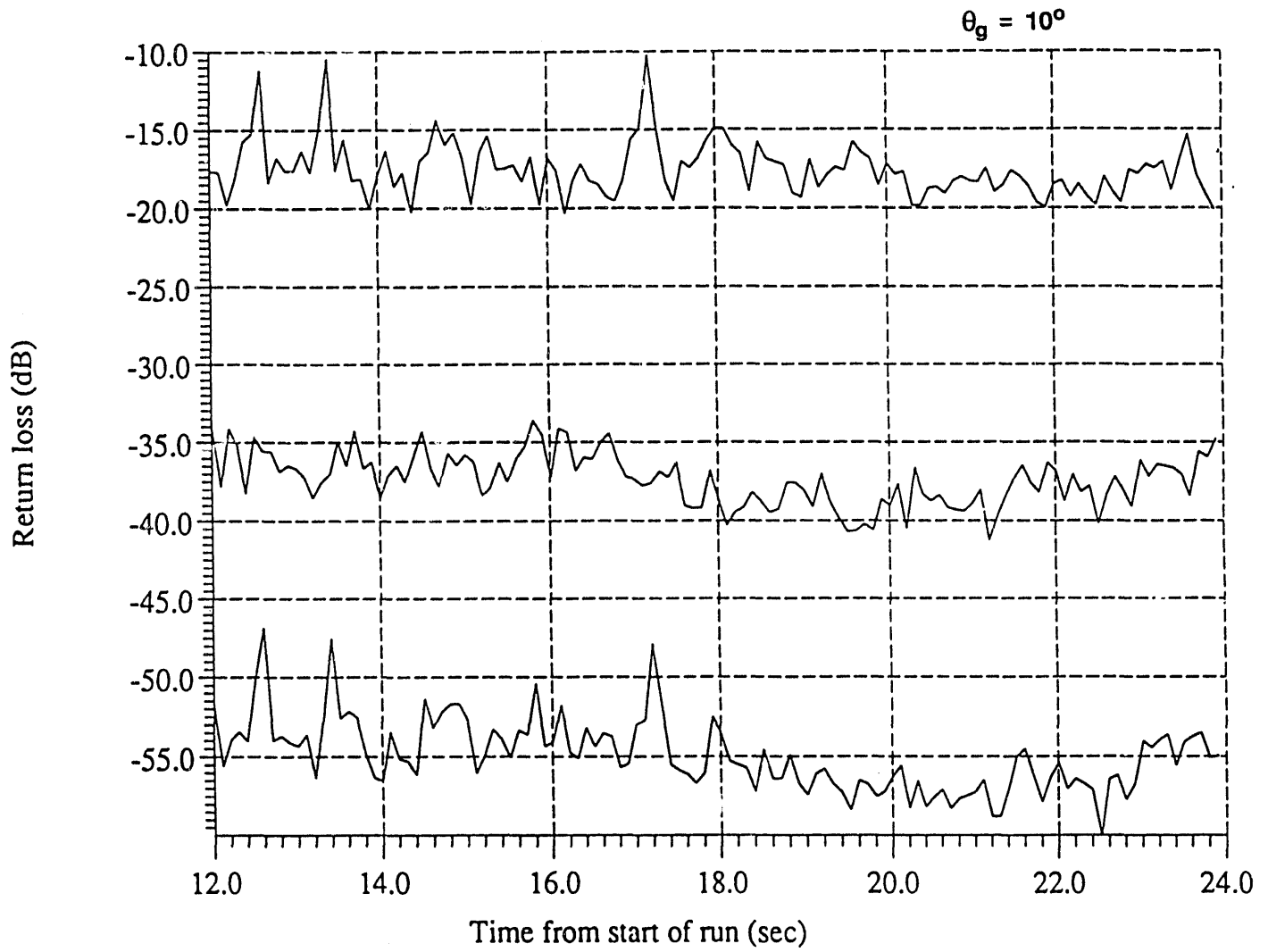


FIG. 8 A short sample of time-resolved, band-pass filtered Slow signals; against-wind look direction,  $\theta_g = 10^\circ$ . HH is the bottom trace, VV is the middle trace, HH/VV (polarization ratio) is the top trace. Note that HH(t) and VV(t) are not well correlated in time. HH/VV *never* exceeds 0 dB.

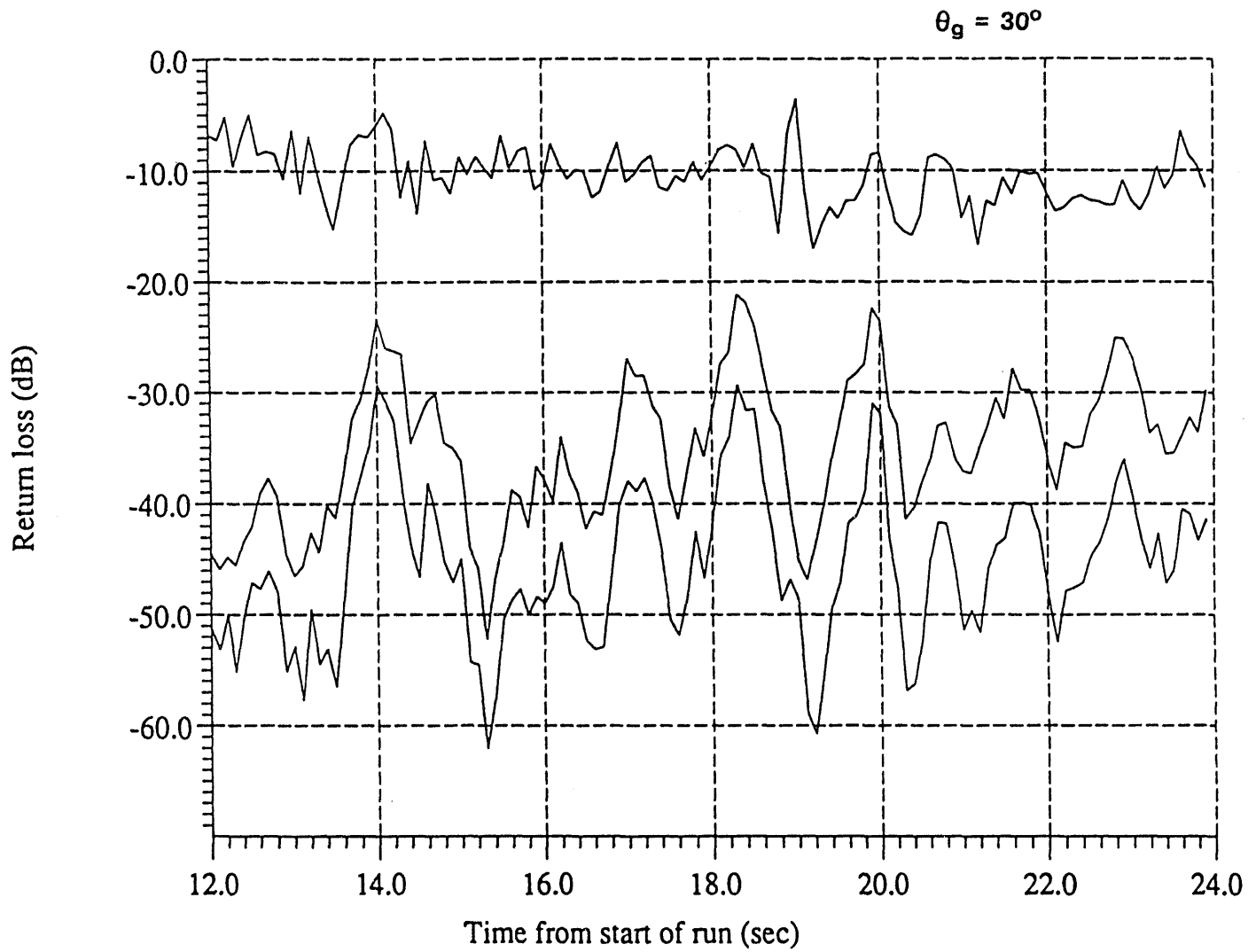


FIG. 9 A short sample of time-resolved, band-pass filtered Slow signals; against-wind look direction,  $\theta_g = 30^\circ$ . HH is the bottom trace, VV is the middle trace, HH/VV is the top trace. Note that HH(t) and VV(t) are much better correlated in time and that HH/VV *never* exceeds 0 dB.

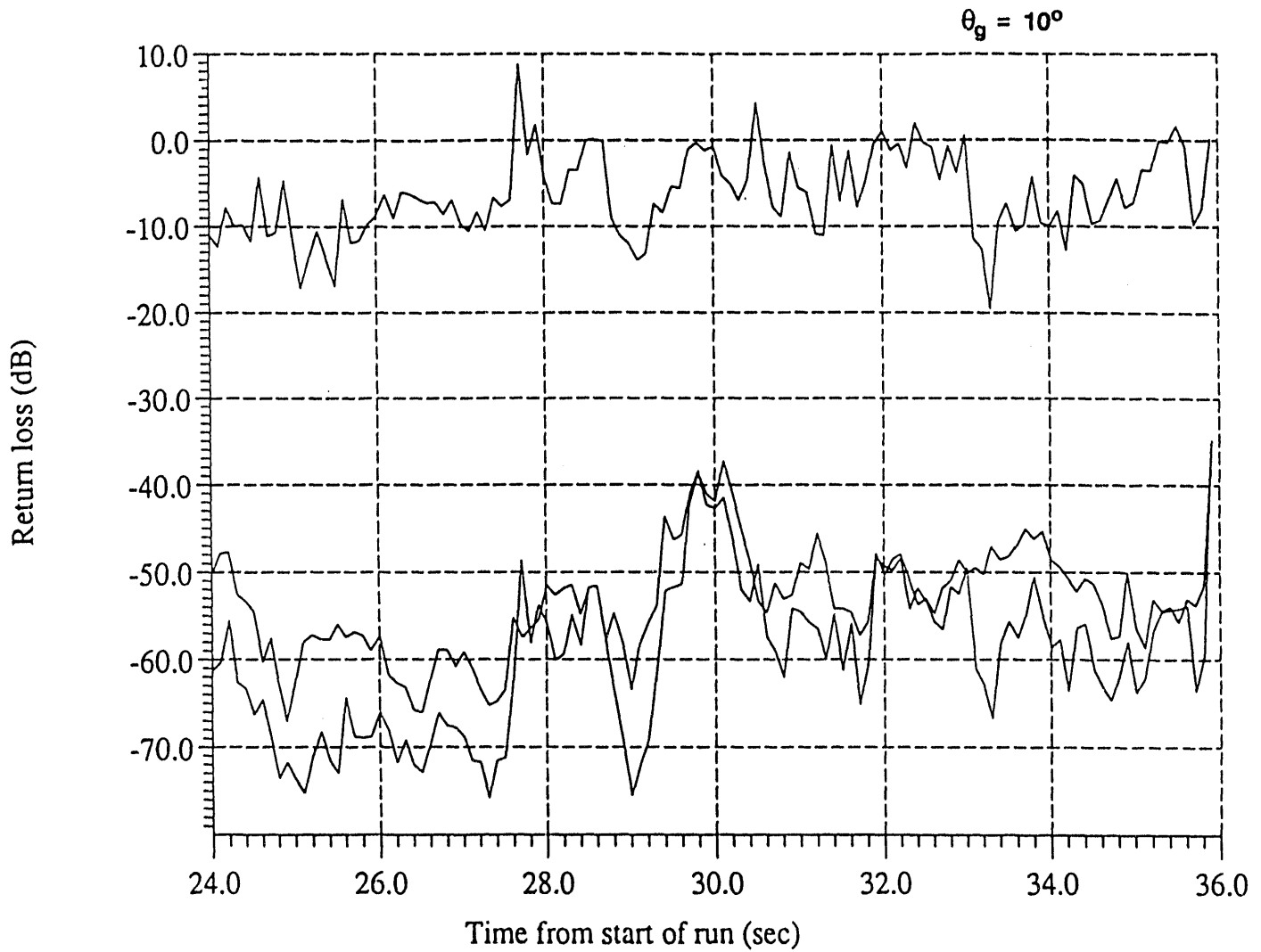


FIG. 10 A short sample of time-resolved, band-pass filtered Fast signals; against-wind look direction,  $\theta_g = 10^\circ$ . HH is the bottom trace, VV is the middle trace, HH/VV is the top trace. Note that HH(t) and VV(t) are not well correlated in time, but better correlated than the case in Fig. 8. Note also that HH/VV occasionally equals or exceeds 0 dB. Also note that fluctuations of HH/VV about the mean value are larger than for the Slow case (Fig. 8).

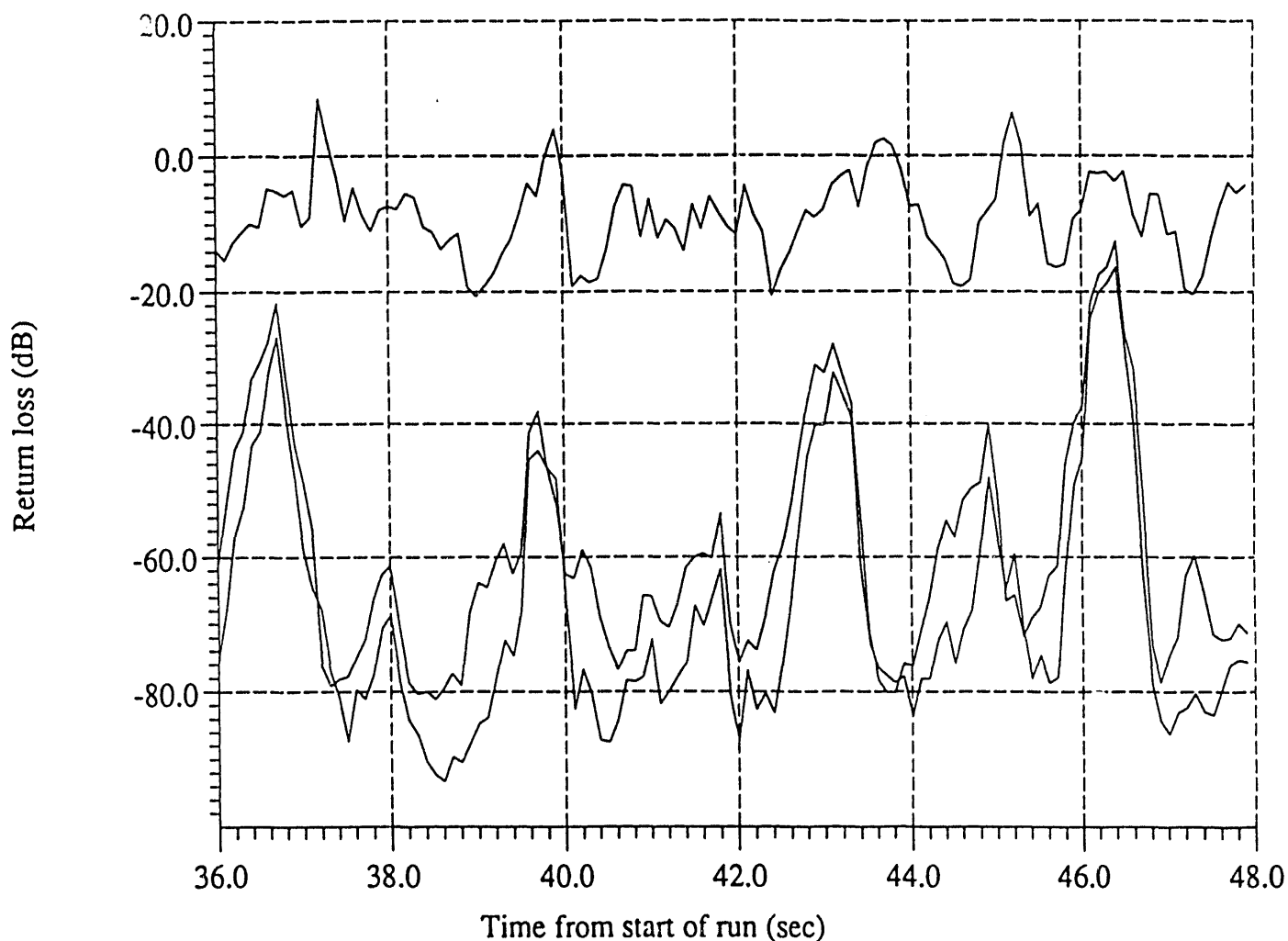
$\theta_g = 35^\circ$ 

FIG. 11 A short sample of time-resolved, band-pass filtered Fast signals; against-wind look direction,  $\theta_g = 35^\circ$ . HH is the bottom trace, VV is the middle trace, HH/VV is the top trace. Note that HH(t) and VV(t) are much better correlated in time. Note that HH/VV occasionally equals or exceeds 0 dB also for this intermediate grazing angle. As a matter of fact, for Fast signals, this occurs for all grazing angles (see text).

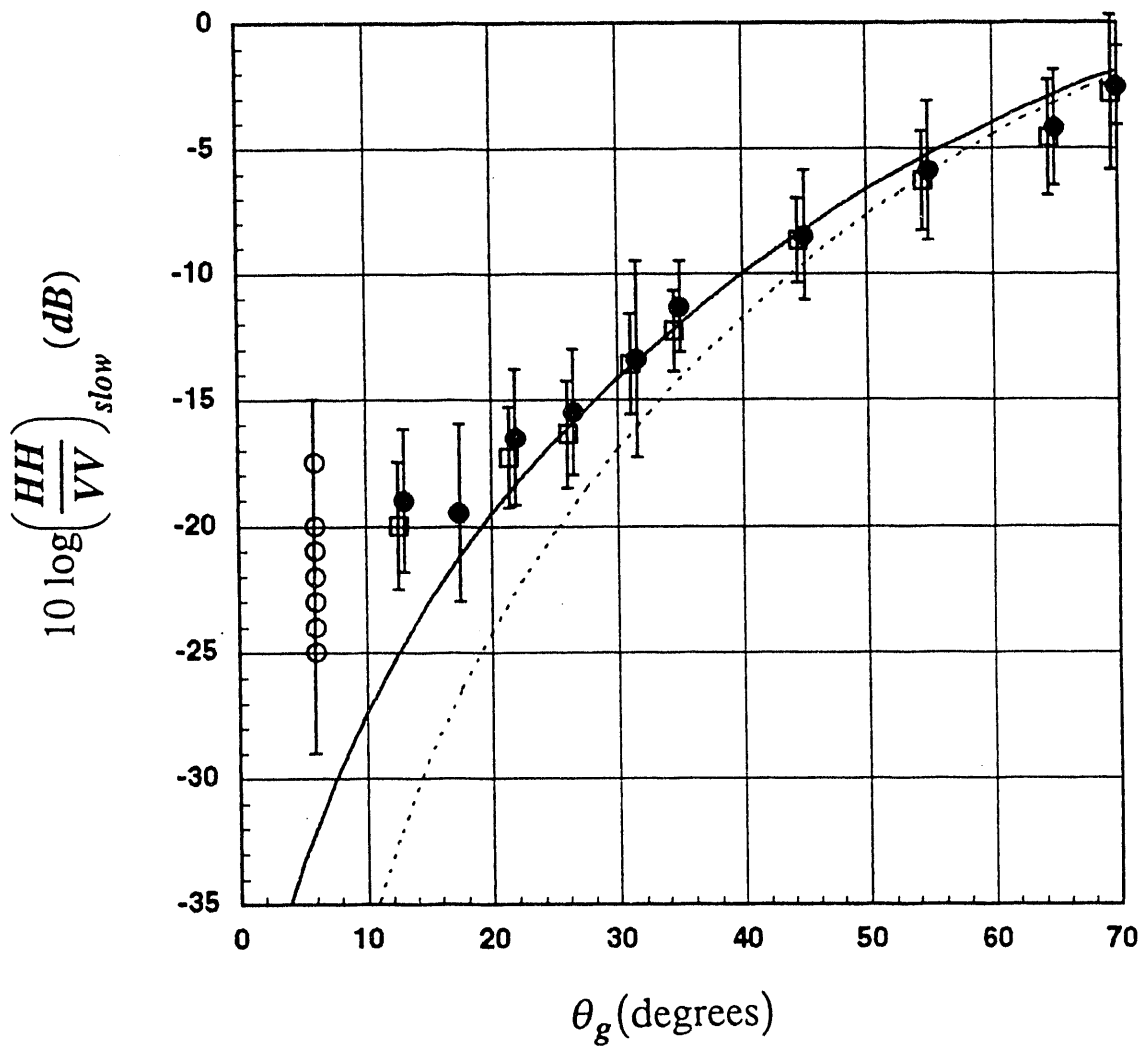
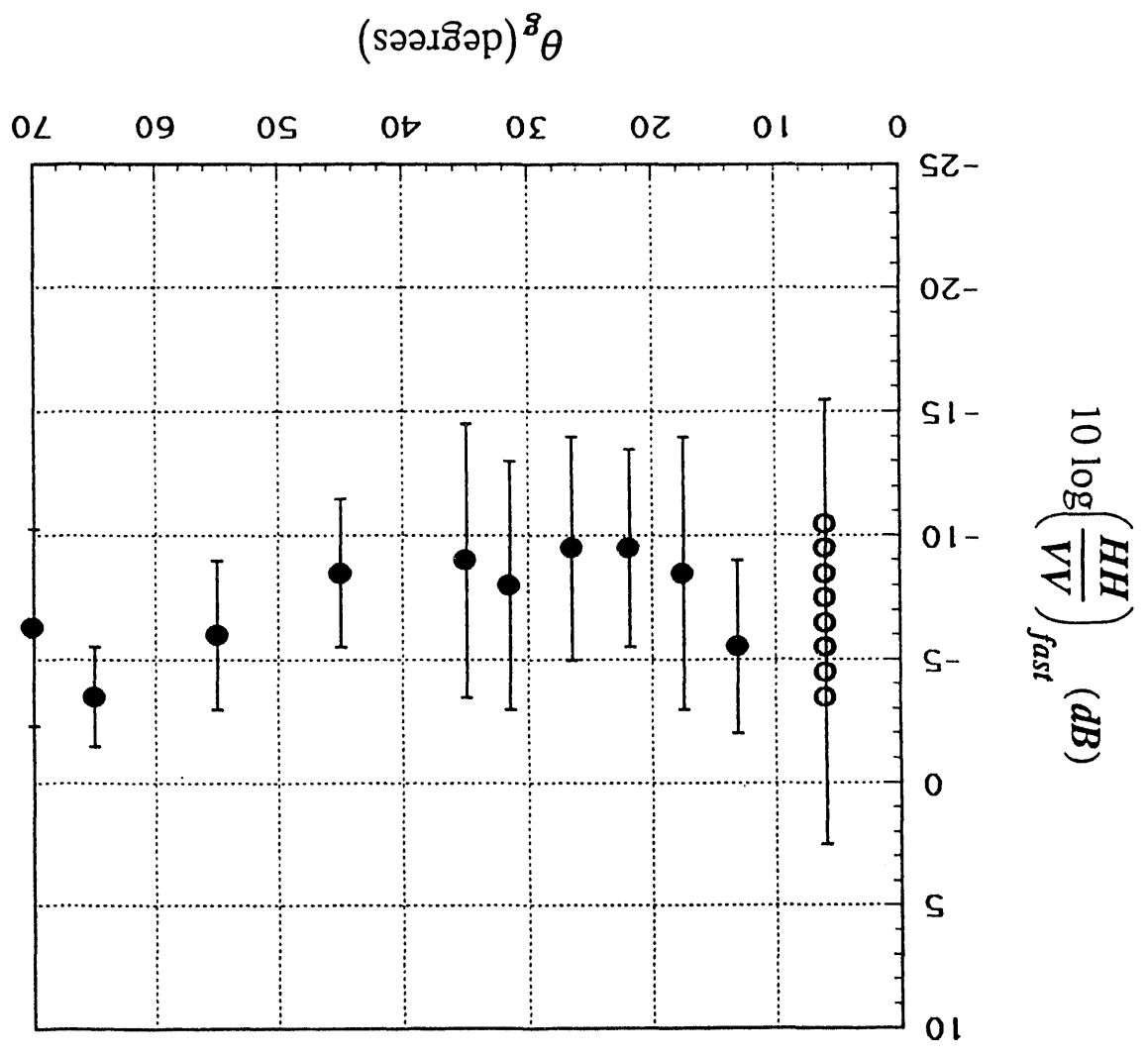


FIG. 12 Time-averaged polarization ratio of Slow signals. Solid circles are TRW against-wind runs, squares are TRW cross-wind runs, hollow circles are RSRE data. The error bar represents one standard deviation above and below the data point. The solid curve is Rice's theory with a dielectric constant appropriate for the water temperature and salinity of Loch Linnhe and the Sound of Sleat ( $\epsilon = 51.4 - i 39.1$ ). The poor agreement of Rice's theory using a *perfect conductor* model is indicated by the dotted curve.

FIG. 13 Time-averaged polarization ratio of Fast signals. Solid circles are TRW against-wind runs, hollow circles are RSRE data. Although there are some physics models, there is no theory, with predictive or postdictive capability, available for Fast signals at present.



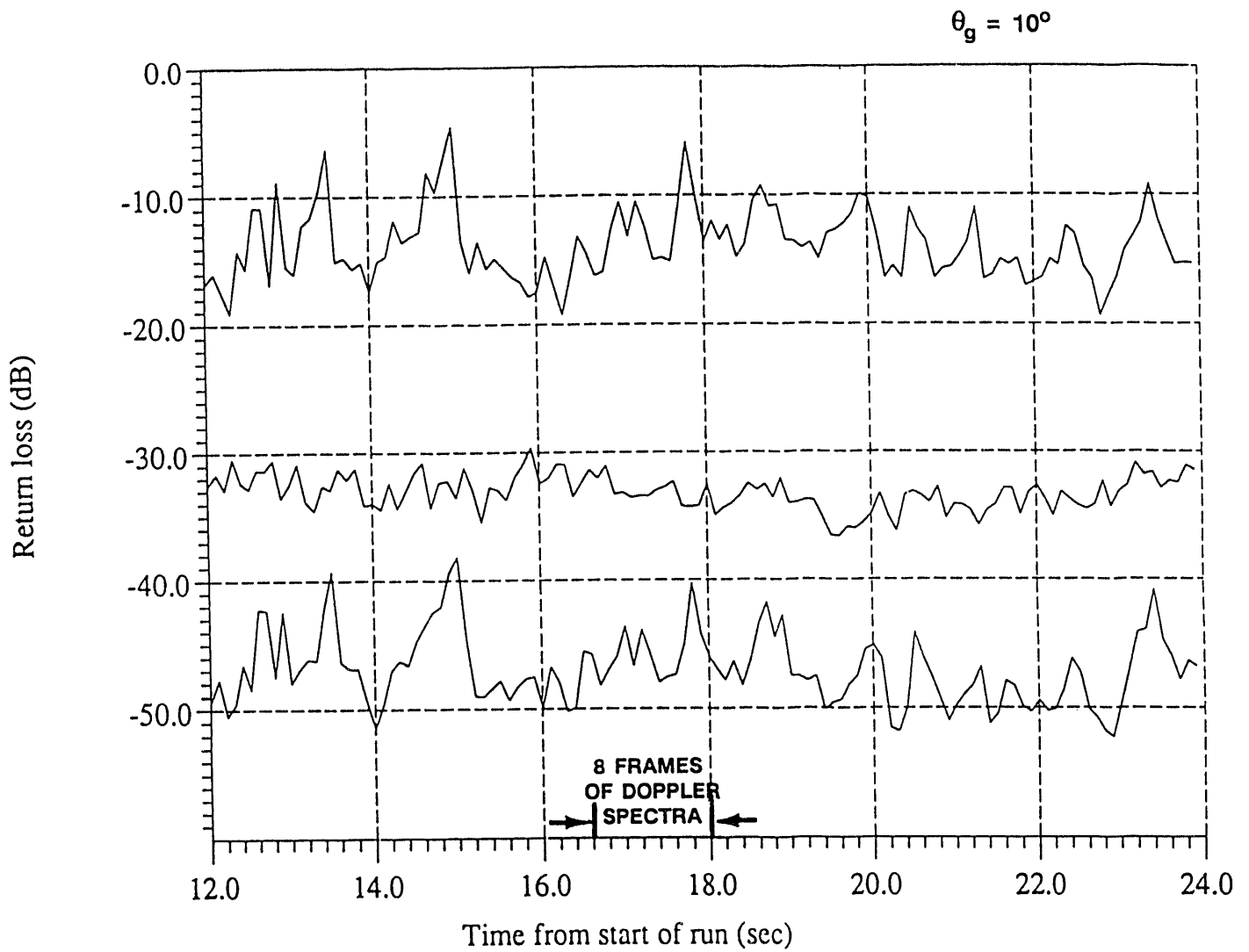


FIG. 14 A 12-second sample record of the total signal for an against-wind run,  $\theta_g = 10^\circ$ . The lower trace is HH, the middle trace is VV and the top trace is HH/VV. Note that HH appears to be spikier. Between the time of 16.6 s to 18.0 s, eight frames of Doppler spectra will be shown in the following Figure.



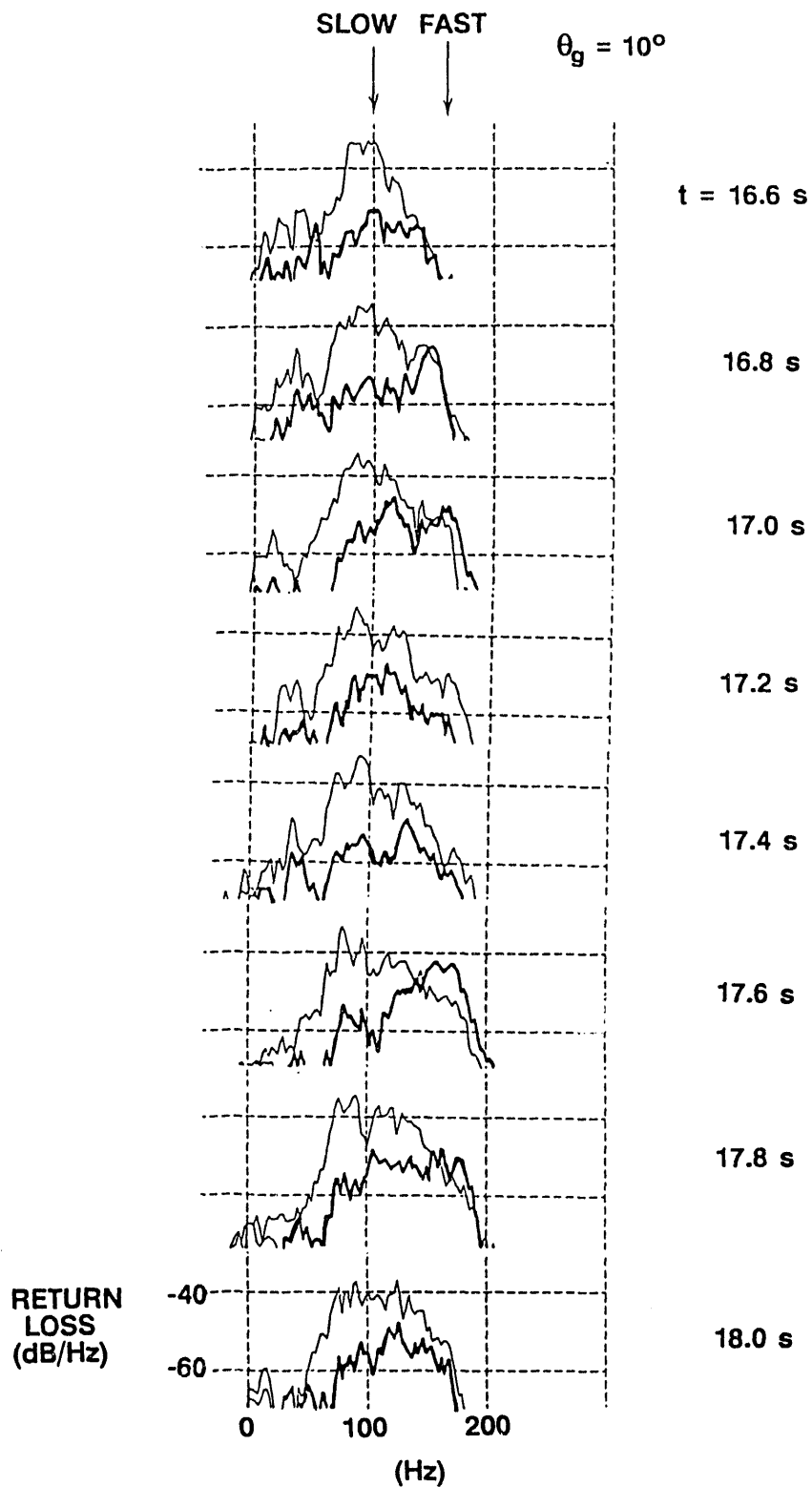


FIG. 15 A sequence of time-resolved Doppler spectra (the heavy curve is HH, the light curve is VV) depicting how horizontal and vertical polarizations occasionally indicate Fast returns. Note that in the Fast region, it is possible for HH to equal or exceed VV. Also note energy in "cascade" frequencies. Refer to text for description.

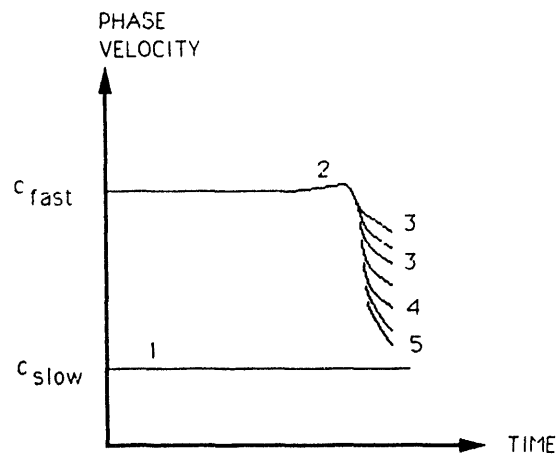
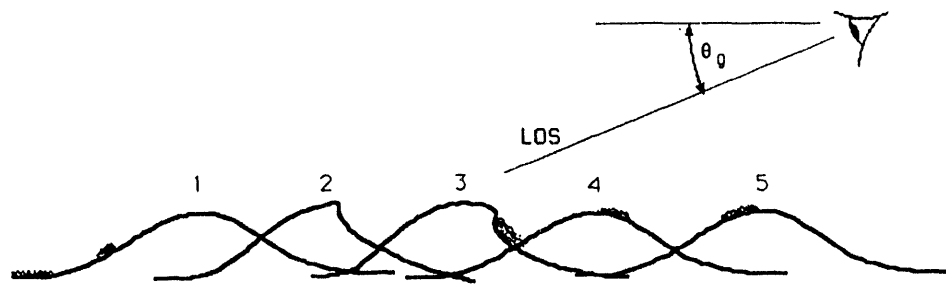


FIG. 16 A possible scenario which can produce the type of Doppler spectra shown in Fig. 15. The top picture is a depiction of the various stages of an incipient wave-breaking process. The evolution of the scatterer speed of the various types of scatterers is given in the bottom "phase velocity vs. time" graph.

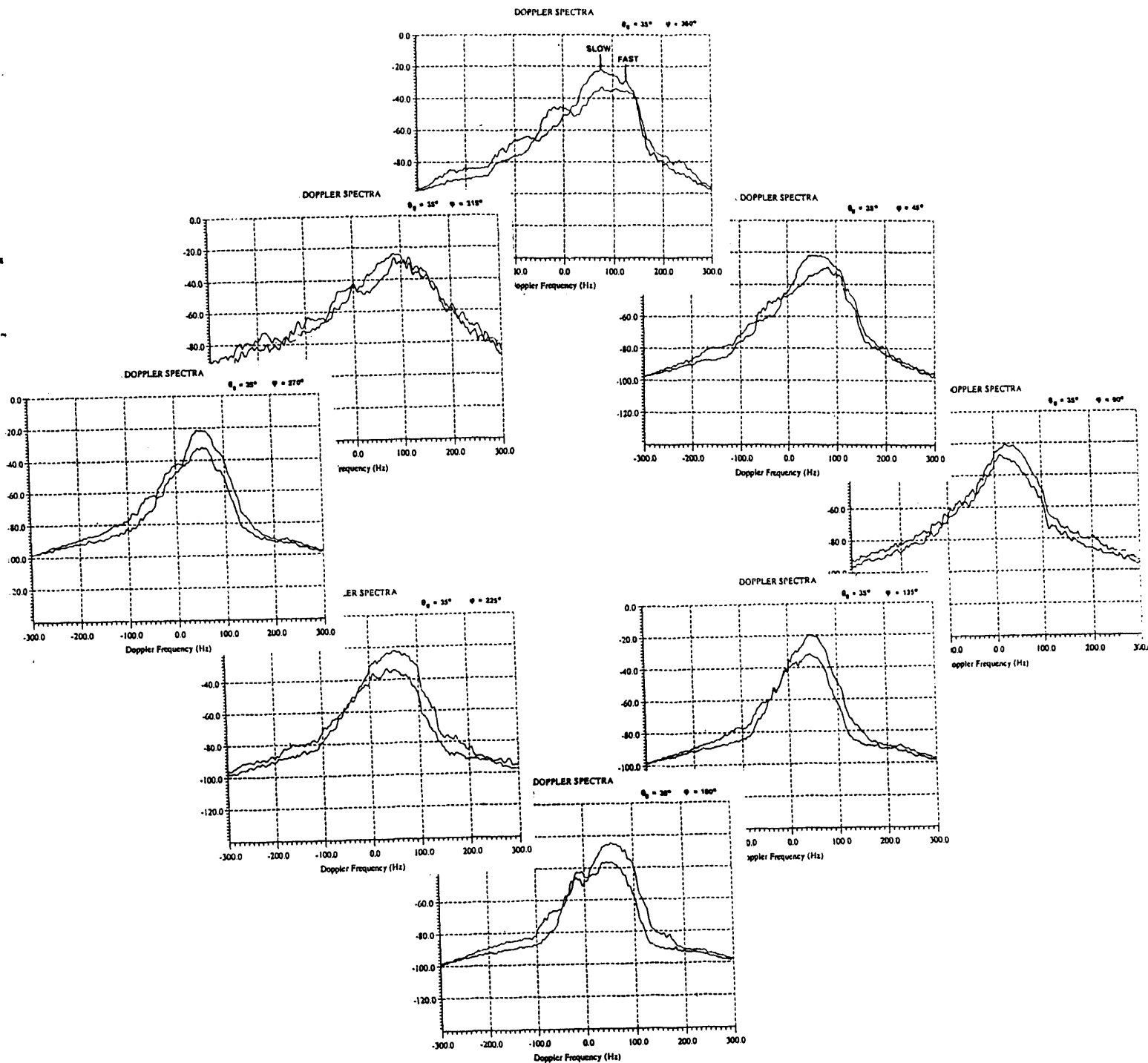


FIG. 17 Doppler spectra as a function of wind direction. This *circle-run* sequence was conducted at a fixed grazing angle of  $\theta_g = 35^\circ$ . Doppler spectra at  $45^\circ$  intervals with respect to the wind direction are shown. The data set starts and ends with the against-wind orientation ( $\varphi = 0^\circ$  and at  $\varphi = 360^\circ$ ). The HH spectrum can always be easily identified as having the lower spectral value at the peak frequency than the VV spectrum.

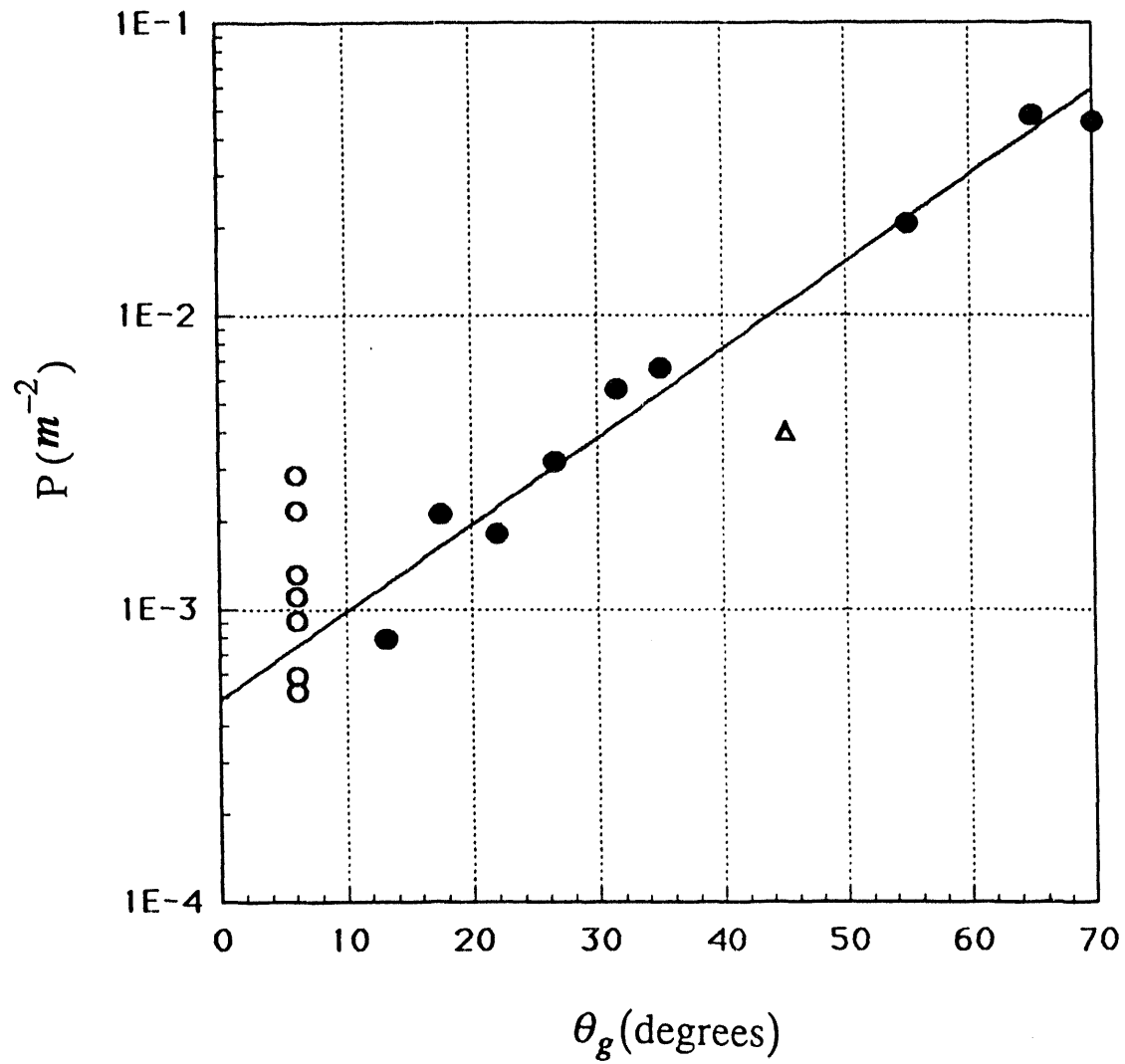


FIG. 18 Probability of "super" events per unit footprint area as a function of grazing angle. Solid circles are TRW data, hollow circles are RSRE data. The triangle is a run at the lowest wind speed. The straight line is a least squares fit to the solid circles.

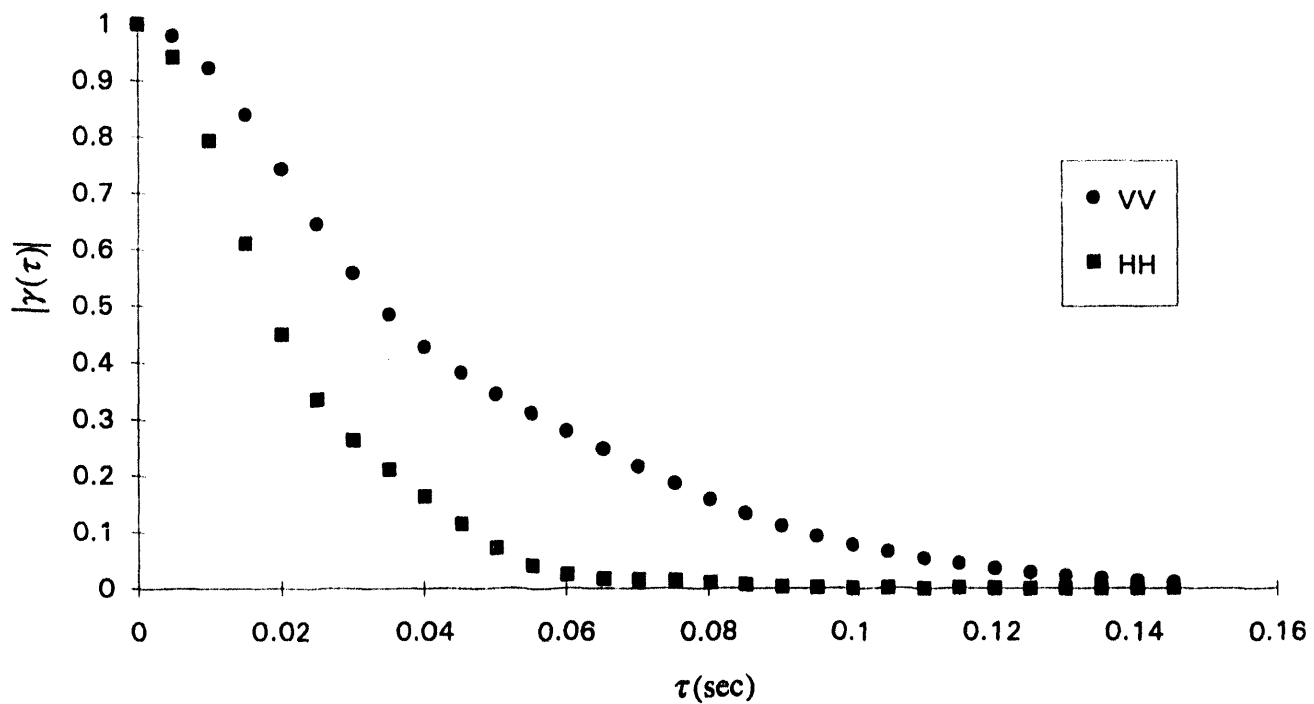


FIG. 19 The normalized autocorrelation functions of the horizontal and vertical polarizations versus lag time. Against-wind look,  $\theta_r = 10^\circ$ . Note that  $|\gamma_{HH}|$  is more exponential-like while  $|\gamma_{VV}|$  is more Gaussian-like.

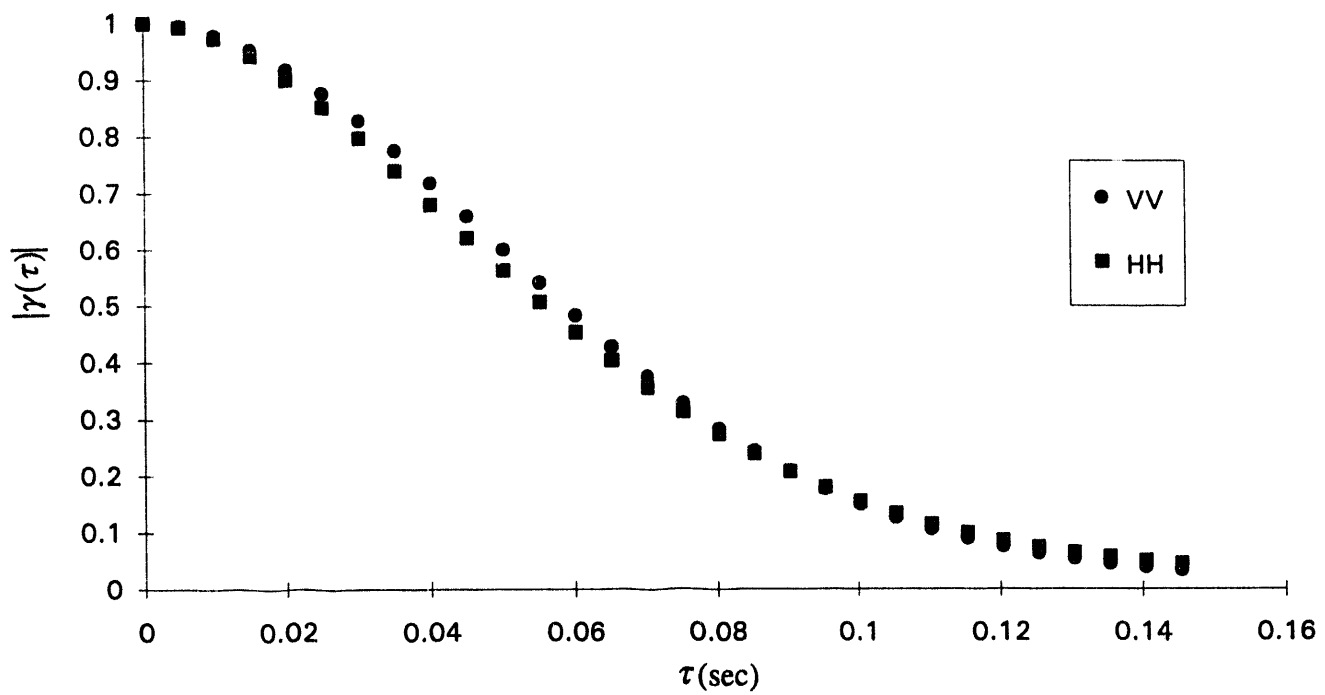


FIG. 20 The normalized autocorrelation functions of the horizontal and vertical polarizations versus lag time. Against-wind look,  $\theta_g = 55^\circ$ . Both  $|\gamma_{HH}|$  and  $|\gamma_{VV}|$  are Gaussian-like and almost identical.

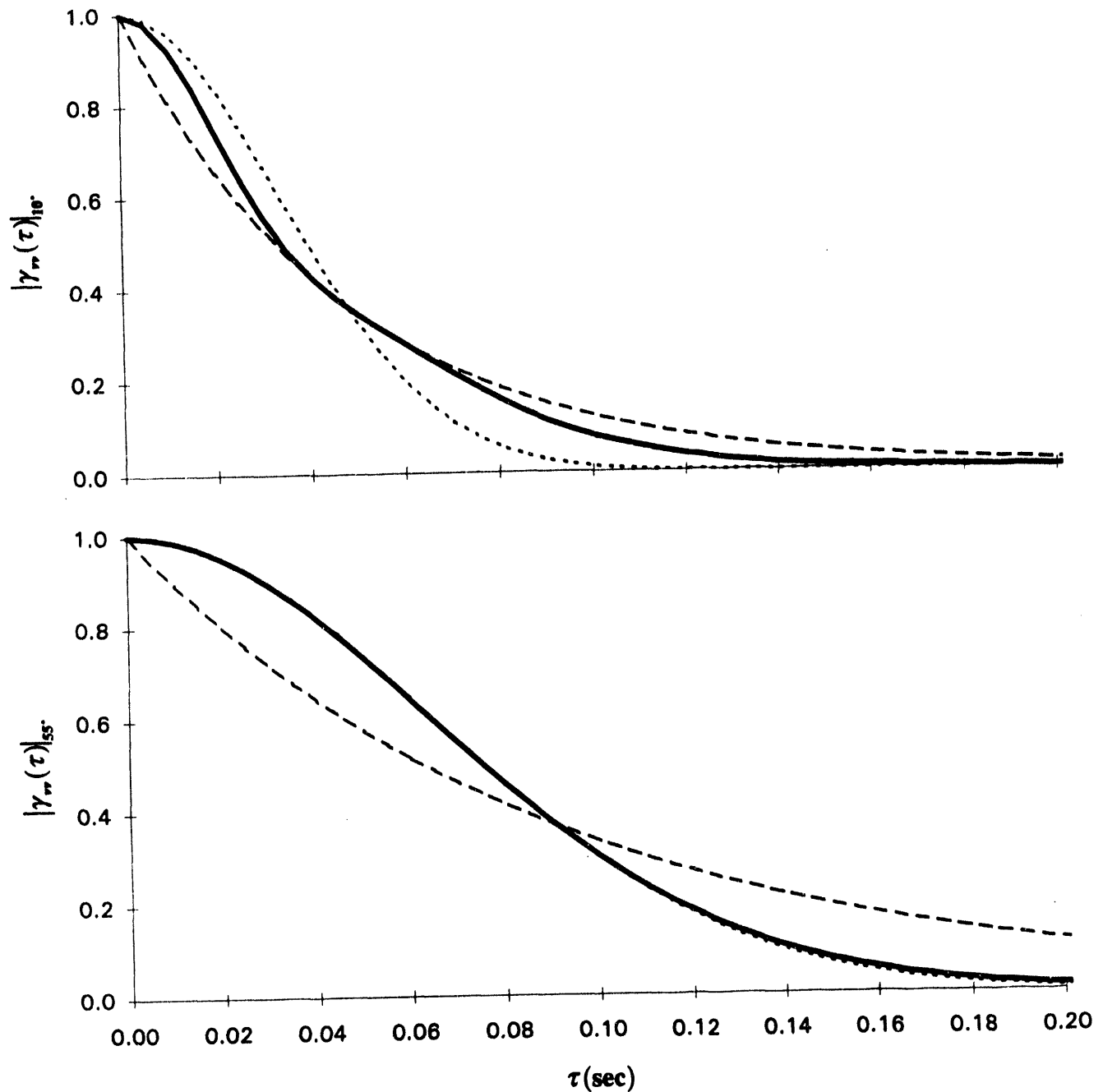


FIG. 21 The quantitative difference between normalized autocorrelation functions for small-grazing-angle against-wind (upper graph) and large-grazing-angle cross-wind (lower graph) cases. The grazing angles are  $10^\circ$  and  $55^\circ$  for the upper and lower graphs, respectively. The solid line represents the experimental data, the *Gaussian model* is represented by the short dashed line while the *exponential model* is represented by the long dashed line. Note that for  $10^\circ$ ,  $|\gamma_w|$  is bracketed between the two model curves, while at  $55^\circ$ ,  $|\gamma_w|$  is practically Gaussian.

**DATE  
FILMED**

**10 / 18 / 94**

**END**



